

Virgo: Scalable Unsupervised Classification of Cosmological Shock Waves

Max Lamparth^{a,c,*}, Ludwig M. Böss^{b,c}, Ulrich Steinwandel^d, Klaus Dolag^{b,e}

^a*Physik-Department, Technische Universität München, James-Franck-Str. 1, Garching, 85748, Germany*

^b*Universitäts-Sternwarte, Fakultät für Physik, Ludwig-Maximilians-Universität München, Scheinerstr. 1, München, 81679, Germany*

^c*Excellence Cluster ORIGINS, Boltzmannstr. 2, Garching, 85748, Germany*

^d*Center for Computational Astrophysics, Flatiron Institute, 162 5th Avenue, New York, 10010, United States of America*

^e*Max-Planck-Institut für Astrophysik, Karl-Schwarzschild-Str. 1, Garching, 85741, Germany*

Abstract

Cosmological shock waves are essential to understanding the formation of cosmological structures. To study them, scientists run computationally expensive high-resolution 3D hydrodynamic simulations. Interpreting the simulation results is challenging because the resulting data sets are enormous, and the shock wave surfaces are hard to separate and classify due to their complex morphologies and multiple shock fronts intersecting. We introduce a novel pipeline, VIRGO, combining physical motivation, scalability, and probabilistic robustness to tackle this unsolved unsupervised classification problem. To this end, we employ kernel principal component analysis with low-rank matrix approximations to denoise data sets of shocked particles and create labeled subsets. We perform supervised classification to recover full data resolution with stochastic variational deep kernel learning. We evaluate on three state-of-the-art data sets with varying complexity and achieve good results. The proposed pipeline runs automatically, has only a few hyperparameters, and performs well on all tested data sets. Our results are promising for large-scale applications, and we highlight now enabled future scientific work.

Keywords: Machine Learning, Deep Learning, Probabilistic Modeling, Kernel Methods, Variational Inference, Clustering, Astrophysics, Cosmology

1. Introduction

Cosmological structures form by gravitationally accreting mass from their surroundings [e.g. 7, 68, 50]. As galaxies and groups of galaxies fall into clusters, they dissipate their energy in the form of shock waves in the diffuse gas between them, labeled as the intra-cluster medium (ICM) [e.g. 15, 56, 57, 76, 77, 62, 71]. Within these systems, the evolution of shock waves is the primary driver that sets the global physical properties of these systems, like the velocity and temperature structure. In addition, shock waves can play a crucial role in the evolution of many other astrophysical systems such as supernova explosions in the Interstellar medium [e.g. 65, 72, 73, 38, 78, 70, 20]. These shock waves are defined as discontinuities in density and temperature, propagating through the hot ($T \sim 10^8$ K) and thin ($\rho \sim 10^{-28}$ g cm $^{-3}$) plasma of the ICM at supersonic speeds. They are among the universe's most powerful accelerators of relativistic protons and electrons (cosmic rays, CRs). Moreover, we can observe them as arc-shaped radio synchrotron emission sources on the outskirts of merging galaxy clusters, millions of lightyears in diameter [75]. The total energy dissipated at these shocks which

*Corresponding author: max.lamparth@tum.de

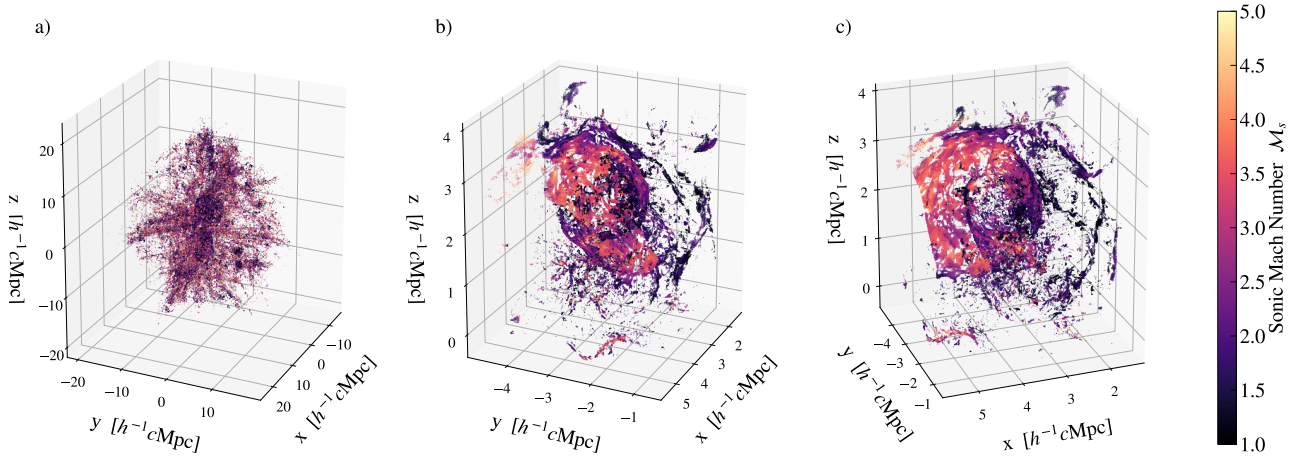


Figure 1: We show a reduced simulated data set CLUSTHD_2 containing all particles with a detected shock in the sonic Mach number range $\mathcal{M}_s \in [1, 5]$. *a)* Full simulation domain. The main cluster is in a cutout of the cosmic web, which shows internal and accretion shocks. *b)* Manual zoom into the cluster showing the complex shock structure of multiple ongoing merger shocks. We want to determine all shock surface particles as separate labeled groups and remove non-shock wave particles. *c)* Same as *b)*, but rotated by 45° .

will subsequently become available for accelerating CR is proportional to the shock speed and surface. As the fraction of shock wave energy available to accelerate CRs is still poorly constrained [36, 35, 25, 11, 12, 61, 26], knowing the total energy budget helps to constrain the theoretical predictions of acceleration efficiency and therefore give preferences to the different formation scenarios. A statistical comparison of large-scale cosmological simulations with large observational campaigns has the potential to better discriminate between the different formation scenarios. Modeling these cosmological systems with state-of-the-art simulations requires $\mathcal{O}(10^6)$ CPU hours and $\mathcal{O}(10^2)$ TB of RAM, only available on modern supercomputers, as there is large degeneracy in the possible geometry and underlying model assumptions. The produced data sets contain up to $\mathcal{O}(10^{10})$ particles, which we need to interpret to make conclusions about formation scenarios. However, shock wave structures in galaxy clusters form highly complex shapes and surfaces (see Fig. 1), and collisions between them can lead to a complex superposition of different shock waves with overlapping geometries. Therefore we can not make a simple, prior connection between in-falling substructure as drivers with the associated parts of the shock surface from first principles. This setup poses a complex unsupervised classification problem for an unknown number of target classes in which we must find, separate, and label coherent shock wave structures in simulated data.

To this end, we propose a novel, physically motivated, and fully scalable machine learning pipeline to solve the outlined unsupervised classification problem. We separate the task and classify a subset of each original unlabeled data set. For the subset classification, we exploit the inherent non-stationarity of the problem with kernel functions for data pre-selection and use Gaussian mixture models [2] to pre-clean the data from unwanted non-shock wave particles. We further use physically motivated kernel functions with kernel principal component analysis [64] and low-rank matrix approximations [18, 60] to map the data set to a favorable feature space. In this feature space, the data is separable with stationary algorithms as the mapping reduces the local density changes of the original data set. To emphasize this, we use a simple agglomerative clustering algorithm with an automatically determined linking length. Finally, we use the labeled subset to train a scalable classifier to use our algorithm on the full data sets. The classifier needs to be able to deal with the complex density changes of the data set. Therefore, we combine the flexibility of the adaptive basis functions of a neural network with the infinite set of fixed basis functions of a Gaussian process kernel in a scalable way for stochastic

variational deep kernel learning (SV-DKL, DKL), as proposed by the authors of [28, 29, 82, 81]. For the first time, we can tackle this previously unsolved problem with our described pipeline and guarantee scalability for current state-of-the-art and future data sets. To the best of our knowledge, this is also the first application of DKL and SV-DKL to an astrophysical task.

2. Background and Related Work

For our work, we focus on distribution-based (Gaussian mixture models (GMM) [2]), connectivity-based (hierarchical clustering, friends-of-friends (FoF) [13]), and density-based spatial clustering (DBSCAN [19]) algorithms. Our problem requires a flexible solution that makes little or no prior assumptions about shapes and the number of target classes and can deal with non-euclidean metrics. We focus on the listed approaches as they offer various degrees of good scalability to large data sets [45] and flexibility. The FoF algorithm is a special case of DBSCAN [40] and is used in astrophysics, e.g., for structure identification [13, 16]. GMM without a Dirichlet prior [2] require prior assumptions about the expected number of classes. Another tool we can use for dimensionality reduction in combination with previously stated algorithms is principal component analysis (PCA) [33].

2.1. Kernel Methods

Kernel functions k are defined as integral operators. Should k fulfill the Mercer condition [63], calculating $k(\mathbf{x}, \mathbf{x}')$ is equivalent to mapping \mathbf{x} and \mathbf{x}' to a feature space via a function ϕ and taking the inner product [63]

$$k(\mathbf{x}, \mathbf{x}') = \langle \phi(\mathbf{x}), \phi(\mathbf{x}') \rangle_\nu.$$

This equivalence is called the *kernel trick*. Since the equivalent mapping of ϕ is primarily non-linear and usually into higher dimensions, we can use kernel functions to make data more separable for a more straightforward classification. Furthermore, we can construct the Gram matrix \mathbf{K} for $K_{ij} = k(\mathbf{x}_i, \mathbf{x}_j)$ with respect to a data set $\mathcal{D}_n = \{\mathbf{x}_1, \dots, \mathbf{x}_n\}$ of size n . Should \mathbf{K} be positive-semi definite (PSD), then k is a valid covariance function and \mathbf{K} the corresponding covariance matrix. We can interpret \mathbf{K} as a similarity matrix because we score each point \mathbf{x}_i to each other point in \mathcal{D}_n by a similarity criterion defined by the kernel function k .

Kernel functions can be stationary, i.e. $k(\mathbf{x}, \mathbf{x}') = k(\mathbf{x} - \mathbf{x}')$, and therefore invariant under spatial displacements. In addition, we can create composite kernels, as a sum, product, or convolution of two kernel functions [63]. Given that k scores points by a similarity criterion, we can interpret composite kernels as combining similarity criteria with logical operators. As the kernel function parameters are related to data-specific characteristics such as length scales, kernel methods offer interpretable parameters. This benefit is unique compared to other machine learning methods and makes them attractive for physics applications [41]. Thus, we can create physically motivated kernel functions with physical parameters and encode physical information like, e.g., symmetry or local density changes of our problem.

The computational complexity of \mathbf{K} scales with $\mathcal{O}(n^2)$. To use kernel functions with large data sets, we can use a low-rank matrix approximation called Nyström approximation [18, 60]. For this, we chose a random subset \mathcal{D}_m of m data points with $m < n$ to represent the data set and calculate the Gram matrix for $K_{ij} = k(\mathbf{x}_i, \mathbf{x}_j)$ with $\mathbf{x}_i \in \mathcal{D}_n = \{\mathbf{x}_1, \dots, \mathbf{x}_n\}$ and $\mathbf{x}_j \in \mathcal{D}_m \subset \mathcal{D}_n$. Furthermore, we can expand regular PCA to non-linear component analysis by constructing \mathbf{K} of our data set and performing PCA on the result [64].

2.2. Gaussian Processes and Stochastic Variational Gaussian Processes

Gaussian processes provide a strong mathematical framework for probabilistic and non-parametric regression and classification [60]. For n observations \mathbf{y} at input locations X , we can use a PSD kernel function and its Gram matrix \mathbf{K} as a covariance matrix and optimize the model parameters by maximizing the marginal log-likelihood

$$\log p(\mathbf{y} \mid X) = -\frac{1}{2}\mathbf{y}^\top \mathbf{K}^{-1} \mathbf{y} - \frac{1}{2} \log |\mathbf{K}| - \frac{n}{2} \log 2\pi. \quad (1)$$

Due to the inversion of \mathbf{K} in Equ. (1), Gaussian processes have a computational complexity of $\mathcal{O}(n^3)$. For classification, the likelihood is non-Gaussian, intractable and therefore needs to be approximated [60]. An approach to increasing Gaussian processes' scalability are stochastic variational Gaussian processes (SVGPs), as outlined by [28, 29, 30]. They combine sparse Gaussian processes [59] with posterior approximation via variational inference [8]. In addition, the approach uses m trainable inducing points X_S with $m < n$, to have X_S and their predictions \mathbf{f}_S summarize the data set. In doing so, the authors enable non-Gaussian likelihoods and stochastic gradient descent optimization on a lower bound of the marginal log-likelihood from Equ. (1). SVGPs achieve a computational complexity of $\mathcal{O}(m^3)$. However, SVGPs are limited to problems where a smaller number of inducing points suffice to represent the data set's details and where regular kernels are expressive enough.

2.3. Stochastic Variational Deep Kernel Learning

To overcome the limits of kernel functions, the authors of [82] introduced scalable deep kernel learning (DKL) to utilize the adaptive basis functions of a neural network (NN). To achieve computational complexity of $\mathcal{O}(n)$ for n training points during inference, they use local kernel interpolation, inducing points, and structure exploiting algebra introduced in [80]. The authors of [82] use the output features of a deep kernel NN as input for a base kernel of a Gaussian process and jointly train the parameters of the deep kernel NN and the base kernel. This approach combines the, e.g., infinite set of fixed basis functions of a radial basis function (RBF) kernel with a set length scale with a fixed set of highly adaptive basis functions of NNs. Thus, the deep kernel NN learns statistical representations from the data set and enables non-euclidean similarity metrics throughout the input space.

The DKL approach was expanded by [81], introducing stochastic variational deep kernel learning (SV-DKL). It allows for stochastic gradient training enabled by variational inference [8] through a marginal log-likelihood lower bound objective. For correlated predictions, the authors feed the outputs of the deep kernel NN into a set of additive base kernels, which they use for independent Gaussian processes. Furthermore, they mix these Gaussian processes linearly to induce correlations and feed the outputs into a softmax likelihood for classification. The SV-DKL model achieves a computational complexity of $\mathcal{O}(m^{1+1/d})$ for fixed inducing points m and input dimensions of our data set d . We apply SV-DKL on data sets with $d = 6$, see Sec. 4.

2.4. Related Astrophysical Applications

Gaussian processes have found applications in astrophysics [66, 74, 47, 42] as well as (S)VP [37, 46]. The authors of [41] suggested SVGP and SV-DKL for large-scale physics simulation interpolation. There have been analytical [67] and deep learning [48, 49] approaches to shock wave and supernovae identification, whereas only [67] did classification. The authors of [79] recently applied support vector machines to the supervised classification of stellar objects. Clustering algorithms are commonly used in astrophysics [13, 87, 21, 55, 54]. Compared to the other outlined models, SV-DKL is the only approach offering Gaussian process non-parametric and statistical benefits, sufficient scalability and flexibility of applied metrics to solve our

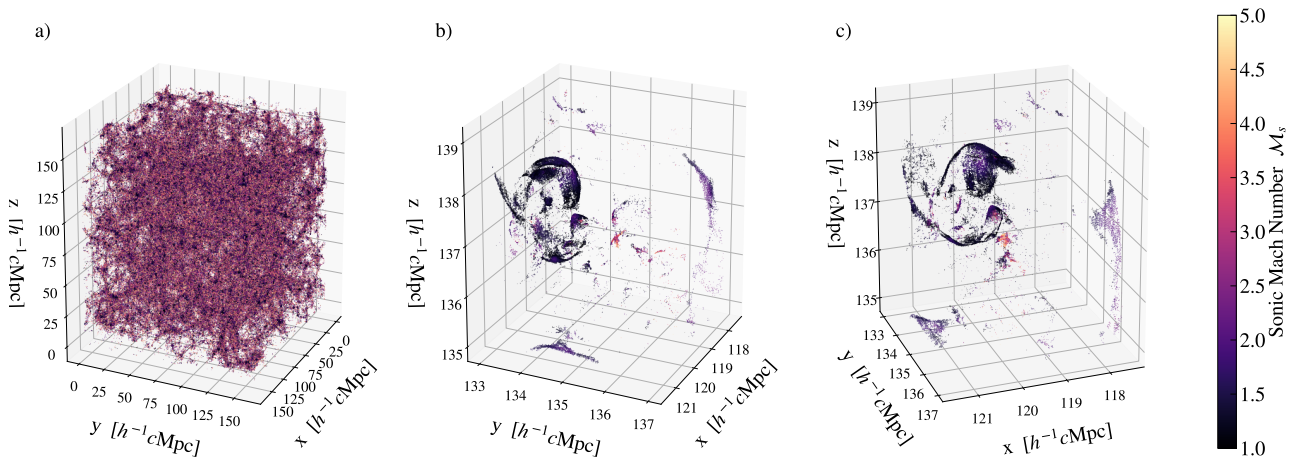


Figure 2: We show a reduced dataset for the BoxMHD simulation, as in Fig. 1. *a)* Full simulation domain. As this is a cosmological box simulation it contains the full cosmic web. *b)* Manual zoom on one of the galaxy clusters forming at the intersection of cosmic filaments. *c)* Same as *b)*, but rotated by 45° .

problem. To the best of our knowledge, this is the first application of DKL and SV-DKL to an astrophysical task. Previous work only hinted at DKL applications [51]. Furthermore, we are not aware of any preceding work having solved this unsupervised classification problem, in particular not with state-of-the-art resolution data sets.

3. Data Sets

We employ three data sets for the shock surface classification to gauge the flexibility of our machine learning pipeline for increasing physical complexity and different scales. The data sets we are using do not contain any personally identifiable information or offensive content.

All data sets were generated with OPENGADGET3, which is an advanced version of P-GADGET3 [69] with an updated SPH scheme [5]. GADGET computes gravity via a tree algorithm [3] and solves for hydrodynamics using smoothed particle hydrodynamics [SPH, 44, 24]. Additionally, we adopt numerical schemes for thermal conduction [e.g. 34, 1], on-the-fly shock detection [4] and a non-ideal magneto-hydrodynamics (MHD) scheme [14, 9]. Different time steps of the same simulation are quasi-independent data sets to be solved due to changing shapes, morphing structures, and a changing number of target classes. We therefore use different time steps of the same simulation as different data sets and indicate them with an index, e.g., during experiments in Sec. 5. We name the data sets as follows:

- CLUSTHD: Ultra-high-resolution hydrodynamics simulation of a single massive galaxy cluster, as shown in Fig. 1.
- CLUSTMHD: Same as CLUSTHD, but expanded to magneto hydrodynamics.
- BoxMHD: High-resolution simulation of a large magneto hydrodynamical cosmological volume with many clusters, as shown in Fig. 2.

CLUSTHD and CLUSTMHD are re-simulations in the cosmological simulation COMPASS and DIANOVA [for a detailed description of the setup see 9] with $\sim 5 \cdot 10^8$ particles¹. CLUSTHD has recently been used to study the interaction of shock waves in the ICM [86]. As CLUSTMHD

¹You can find more information, as well as a movie of the simulation at <http://www.magneticum.org/complements.html#Compass>

also contains magnetic fields, which can lead to additional random motions perpendicular to the shock propagation and a more patchy shock wave surface, it is an ideal case to extend the underlying physical model to probe the robustness of our method. The third data set is a cosmological volume simulation with a box size of 240 Mpc and an effective mass resolution of $\sim 4.5 \cdot 10^6 M_\odot$ which corresponds to 2048^3 particles in the box for the dark matter component and the gas component respectively. We adopt a Planck-cosmology [58] with $\Omega_m = 0.308$, $\Omega_\Lambda = 0.692$, $\Omega_b = 0.049$, $H_0 = 67.81 \text{ km s}^{-1} \text{ Mpc}^{-1}$ and $\sigma_8 = 0.8149$ and generate the initial conditions with the code MUSIC [27] where we use transfer function at redshift 124 computed by CAMB [43]. We adopt a comoving magnetic field of 10^{-14} G at this redshift. We can use this as an effective benchmark for our model to demonstrate performance at a lower resolution but with greater statistical variety.

The three selected data sets allow us to test the performance of VIRGO for shock classification in the most common simulation setups in 3D simulations of galaxy clusters. CLUSTHD and CLUSTMHD consist of single cluster objects, whereas BoxMHD is a simulation of a cosmological volume containing several cluster objects. Therefore, our problem scales from unsupervised classification of an unknown number of target classes from a single cluster to the same for an unknown number of clusters. We reduce the full data set of the simulation to only the parameters relevant for the actual shock surfaces. These are the spatial positions \mathbf{x} , the smoothing length h , the sonic Mach number \mathcal{M}_s detected by the shock finder and the shock normal vector $\hat{\mathbf{n}}_s$ [see 4].

4. VIRGO Model Pipeline

We propose a new analysis pipeline to solve the unsupervised classification of an unknown number of cosmological shock waves in a scalable, probabilistic and physically-motivated way. We separate our approach into four steps:

- 1) For data pre-processing, we remove data points above a conservative velocity threshold ($\mathcal{M}_s \leq 15$) and rescale the data set to a zero mean and unit variance. Large-velocity particles are rarely a part of shock waves surfaces. Our analysis only uses the particle position \mathbf{x} and shock normal vector $\hat{\mathbf{n}}_s$. Each particle therefore is a 6-dimensional vector $\mathbf{q} = (x_x, x_y, x_z, \hat{n}_{sx}, \hat{n}_{sy}, \hat{n}_{sz})^\top$.
- 2) The raw simulation output is noisy with non-shock wave particles and not centered, as is illustrated in Fig. 1a and Fig. 2a. We use an RBF kernel with the Nyström approximation on the particle positions \mathbf{x} with default length scale $l = 2 \cdot \text{Var}(\mathbf{x}) = 2$. We apply PCA on the resulting matrix and use a GMM in the feature space with expectation maximization to separate the actual cluster of shock waves from non-shock wave particles by only accepting the densest GMM component distribution. The density is estimated by particle number and occupied volume. This approach exploits the inherent local density changes of the problem by using a stationary kernel to separate non-shock wave particles from relevant shock wave particles. The step does not reduce the data set through the Nyström approximation, as it works reliably for m as low as 100. We rescale the denoised data again to zero mean and unit variance.
- 3) We construct a physically motivated composite kernel k_V by adding two separate composite kernels made up of Matérn- $\frac{5}{2}$ kernels k_M and linear kernels k_L

$$\begin{aligned} k_1(\mathbf{q}, \mathbf{q}') &= k_M(\mathbf{x}, \mathbf{x}') \cdot k_L(\mathbf{x}, \mathbf{x}') \\ k_2(\mathbf{q}, \mathbf{q}') &= k_M(\mathbf{x}, \mathbf{x}') \cdot k_L(\hat{\mathbf{n}}_s, \hat{\mathbf{n}}'_s) \\ k_V(\mathbf{q}, \mathbf{q}') &= k_1(\mathbf{q}, \mathbf{q}') + k_2(\mathbf{q}, \mathbf{q}'). \end{aligned}$$

The first kernel k_1 creates a non-stationary kernel for spatial information, whereas the second kernel k_2 combines local spatial information with shock normal directions of the particles. We combine k_V with the Nyström approximation but increase m , accepting a reduction of the data set for computational limitations, and finally apply PCA again. The resulting feature space enables separation with a fixed linking length β FoF algorithm. We estimate β with the average n-next-neighbor distance in the resulting feature space. We automatically label every unclassified particle as non-shock wave particle.

4) We use this now labeled subset to train an SV-DKL classifier with a setup as described in Sec. 2.3 and 5. The deep kernel is adjusted to our problem regarding the accuracy and a minimal number of parameters and is a fully connected NN with ReLU activation functions after each layer. We use an RBF kernel for the additive base kernels. The inducing points and training parameters are set up as in [81] and [31], unless stated otherwise in Sec. 5. We use a standard softmax likelihood. With the non-euclidean similarity metric of the deep kernel, we can do long-range extrapolation through our input space with local density changes. This benefit implies a locally adaptable similarity metric required for robust classification. The SV-DKL framework allows us to achieve fast inference and good scalability, as we are not limited by the size of the data set.

Our approach is distinctly scalable, as the proposed pipeline succeeds for data sets of extreme sizes: We can downsize the data set at each step only to recover full resolution with the SV-DKL at the end. We collect our analysis in a Python software package to be available for future analysis, called **VIRGO** (**V**ariational **I**nference package for unsupe**R**vised classification of (inter-)**G**alactic sh**O**ck waves)². The package utilizes already implemented features of PyTorch [52], GPyTorch [22], scikit-learn [53] and pyfof [23]. **VIRGO** has many high-level features for usability, such as a central data class to interact with other **VIRGO** classes. Next to the used models and kernels, we also added tools (plotting, cluster cleaning, result sorting, IO features, and others).

5. Experiments

To test our pipeline, we evaluate on the described data sets from Sec. 3. The generated data sets are the most straightforward data sets available, as this is a complex and previously unsolved problem. As there exist no labeled data sets, it is hard to evaluate the factual accuracy of our pipeline. However, we can verify the goodness of the overall results visually and evaluate our classifier from step 4) in Sec. 4. The results are judged by the coherence of the shock wave surface classification and the removal of obvious non-shock particles. In our studies on all data sets, we can observe that other approaches either over- or under-segment the shock waves, including all mentioned methods in 2 on their own. Some of these studies are presented in the Appendix A.5. The results for the remaining data sets for all steps are also shown in the Appendix A. We optimized all parameters in steps 1) to 3) to run all experiments on a Linux machine with two 2.4 GHz CPU cores and 8 GB RAM to highlight its efficiency. However, step 4) required a GPU with 16 GB RAM.

5.1. Evaluation on CLUSTHD and CLUSTMHD Data Sets

First, we evaluate one single cluster data set where only one shock wave structure is present within many non-shock wave particles. We list any distinct parameters for our pipeline and its training: For the denoising step 2), we use an RBF kernel with the Nyström approximation

²The source code is available at <https://github.com/maxlampe/virgo>

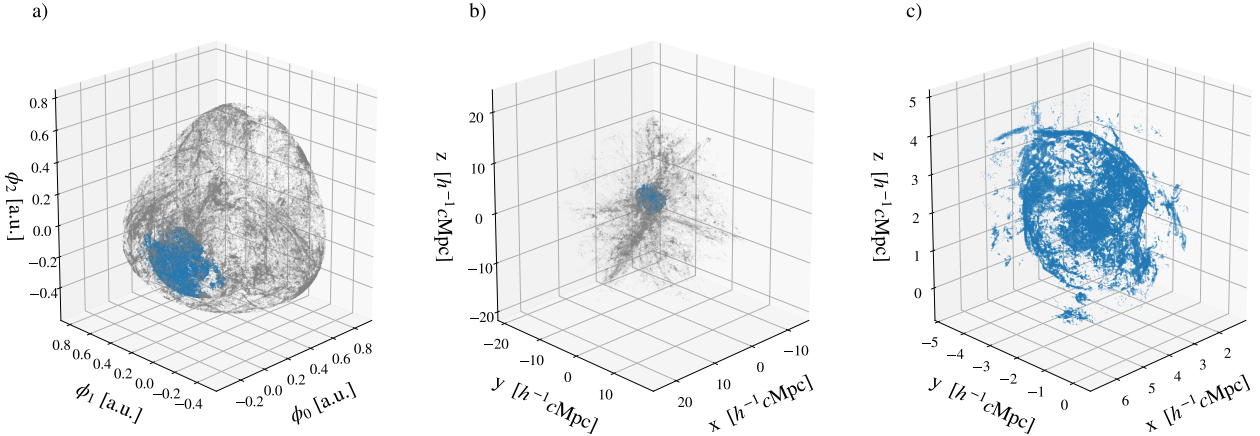


Figure 3: We show the denoising process of Sec. 4 step 2) and its impact on the CLUSTHD₂ data set from Fig. 1. a) GMM fitted in kernel-PCA space with low-density noise component (gray) and high-density cluster component (blue). We only plot the first three kernel space dimensions. b) Labeled data from a), but shown in physical space. c) Resulting denoised data set for further analysis.

$m = 100$, PCA with $k = 5$ components, and GMM with 2 or 5 components, depending on the data set. The physically motivated kernel k_V of step 3) is used with Nyström approximation $m = 500$, PCA with $k = 6$ components, and we estimate the FoF linking length β as the average 20-next-neighbor distance. The deep kernel NN is set up with six input features, $n_h = 1$ hidden layer of size 20, $n_f = 10$ output features, and without pre-training. We trained the SV-DKL of step 4) over 20 epochs, with a batch size of 1024, a grid of 64 inducing points, an overall learning rate of $\alpha = 0.1$, a learning rate scheduler decreasing it by 0.1 after 50 and 75% of the training time, decreased learning rate for the Gaussian process parameters $\alpha_{GP} = \alpha/100$, L2 regularization with weight decay of 10^{-4} , and an ADAM optimizer ($\beta_1 = 0.9$, $\beta_2 = 0.999$) [39]. We employed an 80/10/10 split between training, validation and test sets.

We show the denoising and centering process representative for CLUSTHD₂ in Fig. 3. Our approach accurately separates the dense cluster region from the general simulation output of shocked particles. Should more structures be present in the general output, we increase the number of GMM components and obtain reliable results. In doing so, we achieve good separation for all available and tested data sets, without exception.

We classify the denoised result as described in step 3) with k_V , Nyström approximation, PCA and agglomerative clustering. The resulting classification is illustrated for one data sets in Fig. 4. The figures show the clear separation and classification of the shock surfaces without over-segmentation. Any non-shock-wave particles are labeled as noise with a visibly low error rate. However, this step reduces the data set size to $\mathcal{O}(10^4)$ from the original $\mathcal{O}(10^6)$ after denoising. We recover full resolution with the SV-DKL classifier trained on the labeled subset. Fig. 5 shows the reconstructed and labeled full data set representative of CLUSTHD₂. The complex morphology of the shock waves and its substructures are fully restored.

To compare our classification, we benchmark the SV-DKL against a k-nearest-neighbor (k-NN, $k = 10$) classifier and a fully connected NN. We construct the NN similarly to the deep kernel NN, i.e., one hidden layer of size 20, six input features, and n target classes as output with ReLU activation functions. We present the results in Tab. 1. Next to its other benefits, the SV-DKL outperforms the other methods in terms of accuracy. The authors of [82, 81] further illustrated the (SV)-DKL capabilities compared to other approaches. We expect the SV-DKL to perform better with non-shock wave particles near shock wave surfaces, due to the additive

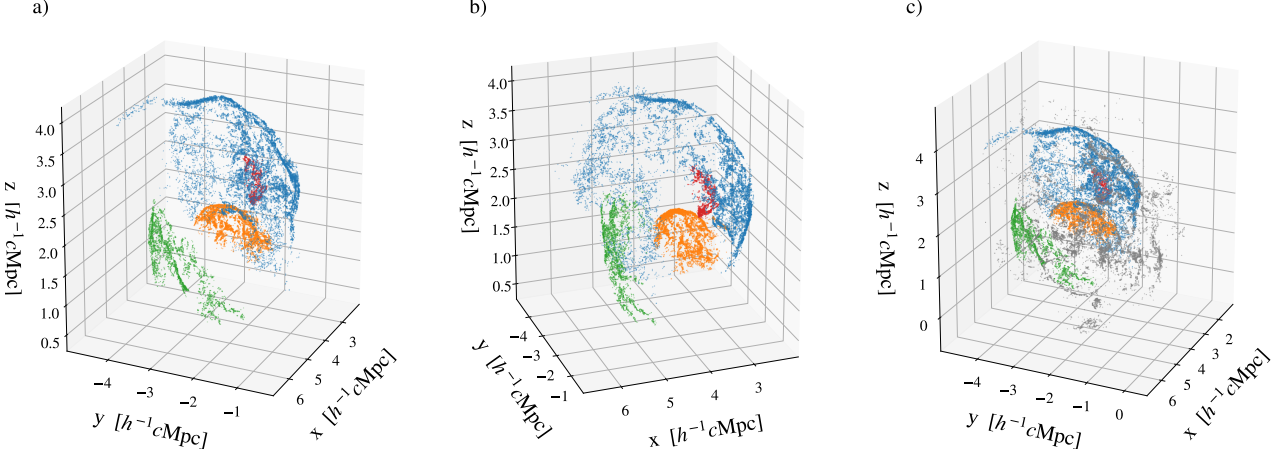


Figure 4: We show the labeled subset of CLUSTHD₂ after the denoising process. The clear separation of the shock wave surfaces from non-shock wave particles (gray) is visible. Also, the estimated error of labeling shock surface particles as non-shock wave particles is visibly negligible. *a)* Labeled subset with the FoF algorithm of step 3) in Sec. 4. *b)* same as a), but rotated by 45°. *c)* Same as a), but with non-shock wave particles plotted too.

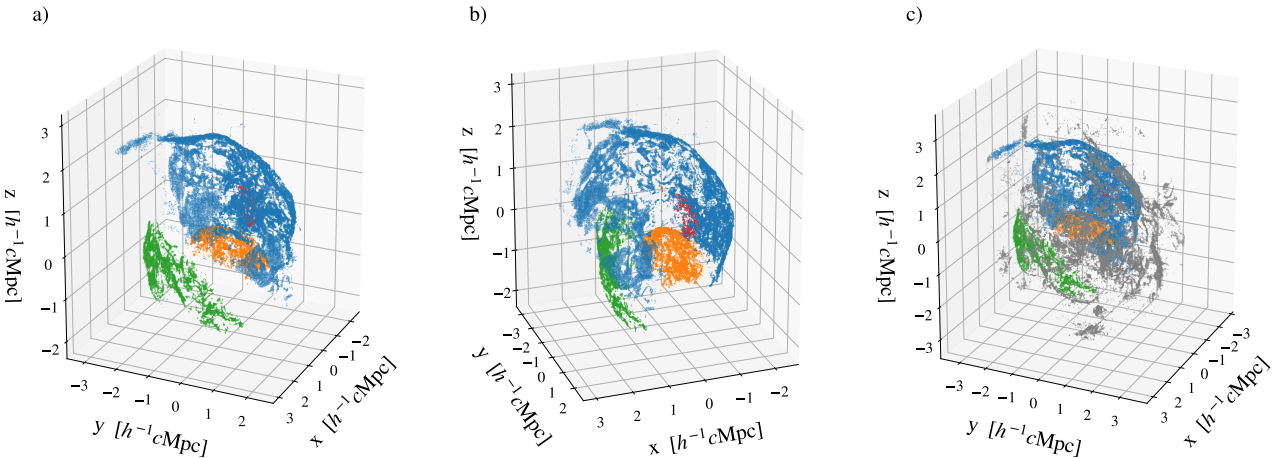


Figure 5: We show the full resolution reconstruction of CLUSTHD₂ with the SV-DKL classification. This result is the final VIRGO output for the raw input in Fig. 1 and allows scalability to large data sets. We state the accuracy of the recovery classification in Tab. 1. *a)* Labeled data set with SV-DKL classifier of step 4) in Sec. 4. *b)* same as a), but rotated by 45°. *c)* Same as a), but with non-shock wave particles.

Gaussian processes. However, k-NN achieves good accuracy regarding the labeled subset. Given the lower hardware requirements of k-NN, we recommend it as a valuable replacement, e.g., for online applications in large-scale simulations.

In addition, VIRGO shows signs of generalization, as we used the trained classifier from the labeled subset of CLUSTHD₂ on the full data set of CLUSTHD₃ and obtained approximately ideal results as well. However, this requires the same amount of target shock wave classes for both data sets. Nevertheless, we can use this for future work for better performance over several time steps by training the SV-DKL on several data sets with similar classes. Furthermore, due to the SV-DKL, VIRGO scales to data sets of any size, given that the underlying model assumptions and inducing points describe the data sets with all facets. For more complex problems, we recommend expanding the expressiveness of the deep kernel with advanced architectures, such as DenseNet [31]. Overall, our proposed pipeline solves the outlined classification problem of cosmological shock waves and delivers robust results.

Table 1: Comparing average test accuracies on the labeled subsets of the data after step 3) in Sec. 4 for different methods on different data sets for ten independent runs. Models are trained from scratch and data sets are re-shuffled. The added index for the data sets indicate a different time step of the simulation. Different time steps of the same simulation are quasi-independent data sets, as the morphologies and number of target classes change from one time step to the next.

Method	CLUSTHD ₁	CLUSTHD ₂	CLUSTHD ₃	CLUSTMHD ₁	BoxMHD ₁
k-NN	97.10 ± 0.34	96.61 ± 0.32	97.19 ± 0.30	96.57 ± 0.39	96.69 ± 0.48
FC-NN	95.33 ± 1.32	95.51 ± 0.84	96.63 ± 0.41	96.19 ± 0.50	95.05 ± 0.69
SV-DKL	97.57 ± 0.54	97.00 ± 0.49	98.36 ± 0.18	98.08 ± 0.16	98.02 ± 0.37

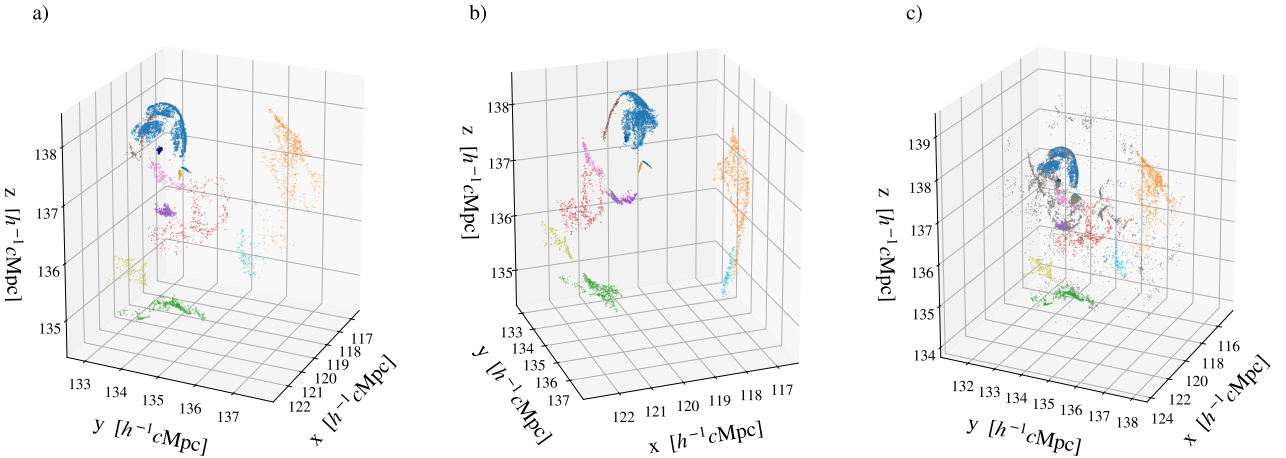


Figure 6: We show the labeled subset of BoxMHD₁ after the additional GMM selection and denoising process. The clear separation of the shock wave surfaces from non-shock wave particles (gray) is visible. Also, the estimated error of labeling shock surface particles as non-shock wave particles is negligible. We set a minimum class size during step 3). Hence, we ignore smaller structures and label them as non-shock wave particles. *a)* Labeled subset with the FoF algorithm of step 3) in Sec. 4. *b*) same as a), but rotated by 45°. *c*) Same as a), but with non-shock wave particles.

5.2. Evaluation on BoxMHD Data Set

To test the extent of VIRGO’s capabilities, we run the pipeline on the more complex BoxMHD data set. All other data sets consist of single cluster objects, whereas BoxMHD is a simulation of a cosmological volume containing several cluster objects. Therefore, we expand our problem of unsupervised classification of an unknown number of target classes from a single cluster to an unknown number of clusters. We repeat step 2) for this data set twice, once with 35 GMM components, keeping the densest ten components, and then again on each remaining component with the parameters described above. This additional step is required to single out dense objects and do single cluster shock wave analysis like in Sec. 5.1. We illustrate the labeling of the subset from step 3) of the biggest substructure in BoxMHD in Fig. 6. The scalability with the SV-DKL works as well as for the other data sets. Some substructures are small enough for data size not to require the SV-DKL, as the Nyström approximation is not required. Overall, VIRGO solves the outlined shock wave classification problem on all tested data sets.

6. Discussion

6.1. Limitations

We determine the FoF linking length estimator from step 3), based on the average n-nearest-neighbor distance in kernel space, to be most prone to error. As can be seen in Fig. 6b, there is a small segment at the top (brown) that should belong to the bigger shock wave surface

(blue). However, our data sets are insufficient to construct a reliable estimator while avoiding overfitting. Another issue to consider is error propagation. Any labeling error in step 3) will be propagated by the SV-DKL. The Gaussian process might correct minor errors for particles close to shock wave surfaces and edges, but this will not correct larger miss classifications. To drive more accurate results and help mitigate the outlined issues, we propose manually creating labeled data sets by experts and generally looking at more simulation data. Furthermore, we think it will be valuable to evaluate test accuracy in points close to the shock wave surfaces. Future work should also verify the robustness of our chosen hyper-parameters on a wider set of simulated data, as this might pose a challenge for users.

For applications to more complex data sets, such as BoxMHD, VIRGO should be combined with a better structure finder. The pipeline successfully classifies shock wave surfaces. However, we should expand the repeated GMM denoising approach from step 2) for cluster finding. The GMM approach will struggle with extensive cosmological simulations, and there is a high risk of discarding smaller clusters. Furthermore, VIRGO currently lacks a criterion to determine whether it found shock waves. We only tested the pipeline on data sets that contained shock wave clusters.

6.2. Impact Statement

We demonstrated the capability of VIRGO for capturing the irregular shapes of shock wave surfaces. Accurately capturing these shock wave surfaces is a critical problem in astrophysics, specifically for particle acceleration at shock fronts which have to be identified *on-the-fly* in large-scale numerical simulations of the Universe at non-negligible compute costs. For future work, we propose using VIRGO to improve galaxy-cluster simulations by increasing the efficiency of particle injections. Furthermore, we recommend applying VIRGO to high-resolution simulations to reconstruct CR acceleration efficiency [as used e.g. in 36] and study properties of shock waves such as Mach number distribution [85]. Future work could use VIRGO to identify morphologically interesting shock structures, populate them with CRs spectra in post-processing and trace their time evolution using a Fokker-Planck solver [e.g. 17, 84, 83, 10]. As these solvers require a substantial amount of memory, applying them to a subset of the simulation is a promising compromise. Beyond studying shock waves in clusters, we expect that VIRGO itself or by extent similar pipelines will enable machine learning applications to study supernovae remnants [32] or general structure finding [e.g. 6].

We believe our proposed pipeline will increase progress in cosmology simulation studies and lead to new applications in astrophysics. While our approach is unique and distinct, it is limited to specific synthetic data sets which are generated and therefore don't necessitate privacy or fairness considerations. Hence, we think a broader impact discussion is not applicable. Furthermore, given our specific data structure (spatial points and shock normal vectors), we see no possible applications outside natural sciences and for other purposes, even with malicious intent. We cannot outline any societal impact beyond scientific interpretations of cosmological structure formation.

6.3. Conclusion

We introduced a novel, physically motivated, and scalable pipeline. The unsupervised classification problem of cosmological shock waves was successfully solved for the first time. We have only begun to explore the possibilities with physically motivated kernel methods combined with variational inference and deep kernel learning in astrophysics, including VIRGO itself. We hope our work inspires other astrophysics and physical sciences applications and that researchers will expand our approach to new problems with advanced kernel architectures or pipeline elements.

Acknowledgements

ML, LMB and KD are acknowledging support by the Deutsche Forschungsgemeinschaft (DFG, German Research Foundation) under Germanys Excellence Strategy – EXC-2094 – 390783311. KD acknowledges support for the COMPLEX project from the European Research Council (ERC) under the European Union’s Horizon 2020 research and innovation program grant agreement ERC-2019-AdG 860744. The hydro-dynamical simulations were carried out at the Leibniz Supercomputer Center (LRZ) in Garching under the project pr86re and the CCA clusters “rusty” located in New York City as well as the cluster “popeye” located at the San Diego Supercomputing center (SDSC). UPS is supported by the Simons Foundation through a Flatiron Research Fellowship at the Center for Computational Astrophysics of the Flatiron Institute. The Flatiron Institute is supported by the Simons Foundation.

References

- [1] Alexander Arth, Klaus Dolag, Alexander M. Beck, Margarita Petkova, and Harald Lesch. Anisotropic thermal conduction in galaxy clusters with MHD in Gadget. *arXiv e-prints*, art. arXiv:1412.6533, December 2014.
- [2] David Barber. *Bayesian reasoning and machine learning*. Cambridge University Press, 2012.
- [3] Josh Barnes and Piet Hut. A hierarchical $O(N \log N)$ force-calculation algorithm. *Nature*, 324(6096):446–449, December 1986. doi: 10.1038/324446a0.
- [4] A. M. Beck, K. Dolag, and J. M. F. Donnert. Geometrical on-the-fly shock detection in smoothed particle hydrodynamics. *MNRAS*, 458(2):2080–2087, May 2016. doi: 10.1093/mnras/stw487.
- [5] A. M. Beck, G. Murante, A. Arth, R. S. Remus, A. F. Teklu, J. M. F. Donnert, S. Pianelles, M. C. Beck, P. Förster, M. Imgrund, K. Dolag, and S. Borgani. An improved SPH scheme for cosmological simulations. *MNRAS*, 455(2):2110–2130, January 2016. doi: 10.1093/mnras/stv2443.
- [6] Peter S. Behroozi, Risa H. Wechsler, and Hao-Yi Wu. The ROCKSTAR Phase-space Temporal Halo Finder and the Velocity Offsets of Cluster Cores. *ApJ*, 762(2):109, January 2013. doi: 10.1088/0004-637X/762/2/109.
- [7] Edmund Bertschinger. Simulations of structure formation in the universe. *Annual Review of Astronomy and Astrophysics*, 36(1):599–654, 1998. doi: 10.1146/annurev.astro.36.1.599. URL <https://doi.org/10.1146/annurev.astro.36.1.599>.
- [8] David M Blei, Alp Kucukelbir, and Jon D McAuliffe. Variational inference: A review for statisticians. *Journal of the American statistical Association*, 112(518):859–877, 2017.
- [9] A. Bonafede, K. Dolag, F. Stasyszyn, G. Murante, and S. Borgani. A non-ideal magnetohydrodynamic gadget: simulating massive galaxy clusters. *Monthly Notices of the Royal Astronomical Society*, 418(4):2234–2250, 12 2011. ISSN 0035-8711. doi: 10.1111/j.1365-2966.2011.19523.x. URL <https://doi.org/10.1111/j.1365-2966.2011.19523.x>.
- [10] Ludwig M. Böss, Ulrich P. Steinwandel, Klaus Dolag, and Harald Lesch. CRESCENDO: An on-the-fly Fokker-Planck Solver for Spectral Cosmic Rays in Cosmological Simulations. *arXiv e-prints*, art. arXiv:2207.05087, July 2022.
- [11] D. Caprioli and A. Spitkovsky. Simulations of Ion Acceleration at Non-relativistic Shocks. I. Acceleration Efficiency. *ApJ*, 783(2):91, March 2014. doi: 10.1088/0004-637X/783/2/91.
- [12] Damiano Caprioli, Horace Zhang, and Anatoly Spitkovsky. Diffusive shock re-acceleration. *Journal of Plasma Physics*, 84(3), may 2018. doi: 10.1017/s0022377818000478.

- [13] Marc Davis, George Efstathiou, Carlos S Frenk, and Simon DM White. The evolution of large-scale structure in a universe dominated by cold dark matter. *The Astrophysical Journal*, 292:371–394, 1985.
- [14] K. Dolag and F. Stasyszyn. An MHD GADGET for cosmological simulations. *MNRAS*, 398(4):1678–1697, October 2009. doi: 10.1111/j.1365-2966.2009.15181.x.
- [15] K. Dolag, F. Vazza, G. Brunetti, and G. Tormen. Turbulent gas motions in galaxy cluster simulations: the role of smoothed particle hydrodynamics viscosity. *MNRAS*, 364(3):753–772, December 2005. doi: 10.1111/j.1365-2966.2005.09630.x.
- [16] K. Dolag, S. Borgani, G. Murante, and V. Springel. Substructures in hydrodynamical cluster simulations. *MNRAS*, 399(2):497–514, October 2009. doi: 10.1111/j.1365-2966.2009.15034.x.
- [17] J. Donnert and G. Brunetti. An efficient Fokker-Planck solver and its application to stochastic particle acceleration in galaxy clusters. *MNRAS*, 443(4):3564–3577, October 2014. doi: 10.1093/mnras/stu1417.
- [18] Petros Drineas, Michael W Mahoney, and Nello Cristianini. On the nyström method for approximating a gram matrix for improved kernel-based learning. *journal of machine learning research*, 6(12), 2005.
- [19] Martin Ester, Hans-Peter Kriegel, Jörg Sander, Xiaowei Xu, et al. A density-based algorithm for discovering clusters in large spatial databases with noise. In *kdd*, volume 96, pages 226–231, 1996.
- [20] Drummond Fielding, Eliot Quataert, Davide Martizzi, and Claude-André Faucher-Giguère. How supernovae launch galactic winds? *MNRAS*, 470(1):L39–L43, September 2017. doi: 10.1093/mnrasl/slx072.
- [21] Bin Fu, Kai Ren, Julio López, Eugene Fink, and Garth Gibson. Discfinder: A data-intensive scalable cluster finder for astrophysics. In *Proceedings of the 19th ACM International Symposium on High Performance Distributed Computing*, pages 348–351, 2010.
- [22] Jacob R. Gardner, Geoff Pleiss, David Bindel, Kilian Q. Weinberger, and Andrew Gordon Wilson. GPyTorch: Blackbox matrix-matrix gaussian process inference with GPU acceleration. *CoRR*, abs/1809.11165, 2018. URL <http://arxiv.org/abs/1809.11165>.
- [23] Simon Gibbons. pyfof - friends of friends cluster finding in python, 2019. URL <https://github.com/simongibbons/pyfof>.
- [24] R. A. Gingold and J. J. Monaghan. Smoothed particle hydrodynamics: theory and application to non-spherical stars. *MNRAS*, 181:375–389, November 1977. doi: 10.1093/mnras/181.3.375.
- [25] Xinyi Guo, Lorenzo Sironi, and Ramesh Narayan. NON-THERMAL ELECTRON ACCELERATION IN LOW MACH NUMBER COLLISIONLESS SHOCKS. i. PARTICLE ENERGY SPECTRA AND ACCELERATION MECHANISM. *The Astrophysical Journal*, 794(2):153, oct 2014. doi: 10.1088/0004-637x/794/2/153.
- [26] Ji-Hoon Ha, Sunjung Kim, Dongsu Ryu, and Hyesung Kang. Effects of Multiscale Plasma Waves on Electron Preacceleration at Weak Quasi-perpendicular Intracluster Shocks. *ApJ*, 915(1):18, July 2021. doi: 10.3847/1538-4357/abfb68.
- [27] Oliver Hahn and Tom Abel. Multi-scale initial conditions for cosmological simulations. *MNRAS*, 415(3):2101–2121, August 2011. doi: 10.1111/j.1365-2966.2011.18820.x.
- [28] James Hensman, Nicolo Fusi, and Neil D Lawrence. Gaussian processes for big data. *arXiv preprint arXiv:1309.6835*, 2013.

[29] James Hensman, Alexander Matthews, and Zoubin Ghahramani. Scalable variational gaussian process classification. In *Artificial Intelligence and Statistics*, pages 351–360. PMLR, 2015.

[30] James Hensman, Alexander G Matthews, Maurizio Filippone, and Zoubin Ghahramani. Mcmc for variationally sparse gaussian processes. *Advances in Neural Information Processing Systems*, 28, 2015.

[31] Gao Huang, Zhuang Liu, Laurens Van Der Maaten, and Kilian Q Weinberger. Densely connected convolutional networks. In *Proceedings of the IEEE conference on computer vision and pattern recognition*, pages 4700–4708, 2017.

[32] Hans-Thomas Janka, Florian Hanke, Lorenz Hüdepohl, Andreas Marek, Bernhard Müller, and Martin Obergaulinger. Core-collapse supernovae: Reflections and directions. *Progress of Theoretical and Experimental Physics*, 2012(1):01A309, 2012.

[33] Ian T Jolliffe and Jorge Cadima. Principal component analysis: a review and recent developments. *Philosophical Transactions of the Royal Society A: Mathematical, Physical and Engineering Sciences*, 374(2065):20150202, 2016.

[34] Martin Jubelgas, Volker Springel, and Klaus Dolag. Thermal conduction in cosmological SPH simulations. *MNRAS*, 351(2):423–435, June 2004. doi: 10.1111/j.1365-2966.2004.07801.x.

[35] Hyesung Kang and Dongsu Ryu. Diffusive shock acceleration at cosmological shock waves. *The Astrophysical Journal*, 764(1):95, jan 2013. doi: 10.1088/0004-637x/764/1/95.

[36] Hyesung Kang, Dongsu Ryu, Renyue Cen, and J. P. Ostriker. Cosmological shock waves in the large-scale structure of the universe: Nongravitational effects. *The Astrophysical Journal*, 669(2): 729–740, nov 2007. doi: 10.1086/521717.

[37] Konstantin Karchev, Adam Coogan, and Christoph Weniger. Strong-lensing source reconstruction with variationally optimised gaussian processes. *Monthly Notices of the Royal Astronomical Society*, 2021.

[38] Chang-Goo Kim and Eve C. Ostriker. Momentum Injection by Supernovae in the Interstellar Medium. *ApJ*, 802(2):99, April 2015. doi: 10.1088/0004-637X/802/2/99.

[39] Diederik P Kingma and Jimmy Ba. Adam: A method for stochastic optimization. *arXiv preprint arXiv:1412.6980*, 2014.

[40] YongChul Kwon, Dylan Nunley, Jeffrey P Gardner, Magdalena Balazinska, Bill Howe, and Sarah Loebman. Scalable clustering algorithm for n-body simulations in a shared-nothing cluster. In *International Conference on Scientific and Statistical Database Management*, pages 132–150. Springer, 2010.

[41] Max Lamparth, Mattis Bestehorn, and Bastian Märkisch. Gaussian processes and bayesian optimization for high precision experiments, 2022. URL <https://arxiv.org/abs/2205.07625>.

[42] Florent Leclercq. Bayesian optimization for likelihood-free cosmological inference. *Physical Review D*, 98(6):063511, 2018.

[43] Antony Lewis, Anthony Challinor, and Anthony Lasenby. Efficient computation of CMB anisotropies in closed FRW models. *ApJ*, 538:473–476, 2000. doi: 10.1086/309179.

[44] L. B. Lucy. A numerical approach to the testing of the fission hypothesis. *Astronomical Journal*, 82:1013–1024, December 1977. doi: 10.1086/112164.

[45] Mahmoud A Mahdi, Khalid M Hosny, and Ibrahim Elhenawy. Scalable clustering algorithms for big data: a review. *IEEE Access*, 2021.

[46] Andrew C Miller, Lauren Anderson, Boris Leistedt, John P Cunningham, David W Hogg, and David M Blei. Mapping interstellar dust with gaussian processes. *arXiv preprint arXiv:2202.06797*, 2022.

[47] Christopher J Moore, Christopher PL Berry, Alvin JK Chua, and Jonathan R Gair. Improving gravitational-wave parameter estimation using gaussian process regression. *Physical Review D*, 93(6):064001, 2016.

[48] Nathaniel R Morgan, Svetlana Tokareva, Xiaodong Liu, and Andrew Morgan. A machine learning approach for detecting shocks with high-order hydrodynamic methods. In *AIAA Scitech 2020 Forum*, page 2024, 2020.

[49] Robert Morgan, Brian Nord, Keith Bechtol, SJ González, E Buckley-Geer, A Möller, JW Park, AG Kim, S Birrer, M Aguena, et al. Deepzipper: A novel deep-learning architecture for lensed supernovae identification. *The Astrophysical Journal*, 927(1):109, 2022.

[50] Thorsten Naab and Jeremiah P. Ostriker. Theoretical Challenges in Galaxy Formation. *ARA&A*, 55(1):59–109, August 2017. doi: 10.1146/annurev-astro-081913-040019.

[51] Ji Won Park, Ashley Villar, Yin Li, Yan-Fei Jiang, Shirley Ho, Joshua Yao-Yu Lin, Philip J Marshall, and Aaron Roodman. Inferring black hole properties from astronomical multivariate time series with bayesian attentive neural processes. *arXiv preprint arXiv:2106.01450*, 2021.

[52] Adam Paszke, Sam Gross, Francisco Massa, Adam Lerer, James Bradbury, Gregory Chanan, Trevor Killeen, Zeming Lin, Natalia Gimelshein, Luca Antiga, Alban Desmaison, Andreas Kopf, Edward Yang, Zachary DeVito, Martin Raison, Alykhan Tejani, Sasank Chilamkurthy, Benoit Steiner, Lu Fang, Junjie Bai, and Soumith Chintala. Pytorch: An imperative style, high-performance deep learning library. In *Advances in Neural Information Processing Systems 32*, pages 8024–8035. Curran Associates, Inc., 2019. URL <http://papers.neurips.cc/paper/9015-pytorch-an-imperative-style-high-performance-deep-learning-library.pdf>.

[53] F. Pedregosa, G. Varoquaux, A. Gramfort, V. Michel, B. Thirion, O. Grisel, M. Blondel, P. Prettenhofer, R. Weiss, V. Dubourg, J. Vanderplas, A. Passos, D. Cournapeau, M. Brucher, M. Perrot, and E. Duchesnay. Scikit-learn: Machine learning in Python. *Journal of Machine Learning Research*, 12:2825–2830, 2011.

[54] María Sol Pera, Gabriel Ignacio Perren, A Moitinho, Hugo Daniel Navone, and Ruben Angel Vazquez. pyupmask: an improved unsupervised clustering algorithm. *arXiv preprint arXiv:2101.01660*, 2021.

[55] Gabriel Ignacio Perren, Ruben Angel Vazquez, and Andres Eduardo Piatti. Asteca: Automated stellar cluster analysis. *Astronomy & Astrophysics*, 576:A6, 2015.

[56] C. Pfrommer, T. A. Enßlin, V. Springel, M. Jubelgas, and K. Dolag. Simulating cosmic rays in clusters of galaxies - I. Effects on the Sunyaev-Zel'dovich effect and the X-ray emission. *MNRAS*, 378(2):385–408, June 2007. doi: 10.1111/j.1365-2966.2007.11732.x.

[57] C. Pfrommer, R. Pakmor, K. Schaal, C. M. Simpson, and V. Springel. Simulating cosmic ray physics on a moving mesh. *Monthly Notices of the Royal Astronomical Society*, 465(4):4500–4529, nov 2016. doi: 10.1093/mnras/stw2941.

[58] Planck Collaboration, P. A. R. Ade, N. Aghanim, M. Arnaud, M. Ashdown, J. Aumont, C. Baccigalupi, A. J. Banday, R. B. Barreiro, J. G. Bartlett, N. Bartolo, E. Battaner, R. Battye, K. Benabed, A. Benoît, A. Benoit-Lévy, J. P. Bernard, M. Bersanelli, P. Bielewicz, J. J. Bock, A. Bonaldi, L. Bonavera, J. R. Bond, J. Borrill, F. R. Bouchet, F. Boulanger, M. Bucher, C. Burigana, R. C. Butler, E. Calabrese, J. F. Cardoso, A. Catalano, A. Challinor, A. Chamballu, R. R. Chary, H. C. Chiang, J. Chluba, P. R. Christensen, S. Church, D. L. Clements, S. Colombi, L. P. L. Colombo,

C. Combet, A. Coulais, B. P. Crill, A. Curto, F. Cuttaia, L. Danese, R. D. Davies, R. J. Davis, P. de Bernardis, A. de Rosa, G. de Zotti, J. Delabrouille, F. X. Désert, E. Di Valentino, C. Dickinson, J. M. Diego, K. Dolag, H. Dole, S. Donzelli, O. Doré, M. Douspis, A. Ducout, J. Dunkley, X. Dupac, G. Efstathiou, F. Elsner, T. A. Enßlin, H. K. Eriksen, M. Farhang, J. Fergusson, F. Finelli, O. Forni, M. Frailis, A. A. Fraisse, E. Franceschi, A. Frejsel, S. Galeotta, S. Galli, K. Ganga, C. Gauthier, M. Gerbino, T. Ghosh, M. Giard, Y. Giraud-Héraud, E. Giusarma, E. Gjerløw, J. González-Nuevo, K. M. Górski, S. Gratton, A. Gregorio, A. Gruppuso, J. E. Gudmundsson, J. Hamann, F. K. Hansen, D. Hanson, D. L. Harrison, G. Helou, S. Henrot-Versillé, C. Hernández-Monteagudo, D. Herranz, S. R. Hildebrandt, E. Hivon, M. Hobson, W. A. Holmes, A. Hornstrup, W. Hovest, Z. Huang, K. M. Huffenberger, G. Hurier, A. H. Jaffe, T. R. Jaffe, W. C. Jones, M. Juvela, E. Keihänen, R. Keskitalo, T. S. Kisner, R. Kneissl, J. Knoche, L. Knox, M. Kunz, H. Kurki-Suonio, G. Lagache, A. Lähteenmäki, J. M. Lamarre, A. Lasenby, M. Lattanzi, C. R. Lawrence, J. P. Leahy, R. Leonard, J. Lesgourgues, F. Levrier, A. Lewis, M. Liguori, P. B. Lilje, M. Linden-Vørnle, M. López-Caniego, P. M. Lubin, J. F. Macías-Pérez, G. Maggio, D. Maino, N. Mandolesi, A. Mangilli, A. Marchini, M. Maris, P. G. Martin, M. Martinelli, E. Martínez-González, S. Masi, S. Matarrese, P. McGehee, P. R. Meinhold, A. Melchiorri, J. B. Melin, L. Mendes, A. Mennella, M. Migliaccio, M. Millea, S. Mitra, M. A. Miville-Deschénes, A. Moneti, L. Montier, G. Morgante, D. Mortlock, A. Moss, D. Munshi, J. A. Murphy, P. Naselsky, F. Nati, P. Natoli, C. B. Netterfield, H. U. Nørgaard-Nielsen, F. Noviello, D. Novikov, I. Novikov, C. A. Oxborrow, F. Paci, L. Pagano, F. Pajot, R. Paladini, D. Paoletti, B. Partridge, F. Pasian, G. Patanchon, T. J. Pearson, O. Perdereau, L. Perotto, F. Perrotta, V. Pettorino, F. Piacentini, M. Piat, E. Pierpaoli, D. Pietrobon, S. Plaszczynski, E. Pointecouteau, G. Polenta, L. Popa, G. W. Pratt, G. Prézeau, S. Prunet, J. L. Puget, J. P. Rachen, W. T. Reach, R. Rebolo, M. Reinecke, M. Remazeilles, C. Renault, A. Renzi, I. Ristorcelli, G. Rocha, C. Rossetti, M. Rossetti, G. Roudier, B. Rouillé d'Orfeuil, M. Rowan-Robinson, J. A. Rubiño-Martín, B. Rusholme, N. Said, V. Salvatelli, L. Salvati, M. Sandri, D. Santos, M. Savolainen, G. Savini, D. Scott, M. D. Seiffert, P. Serra, E. P. S. Shellard, L. D. Spencer, M. Spinelli, V. Stolyarov, R. Stompor, R. Sudiwala, R. Sunyaev, D. Sutton, A. S. Suur-Uski, J. F. Sygnet, J. A. Tauber, L. Terenzi, L. Toffolatti, M. Tomasi, M. Tristram, T. Trombetti, M. Tucci, J. Tuovinen, M. Türler, G. Umana, L. Valenziano, J. Valiviita, F. Van Tent, P. Vielva, F. Villa, L. A. Wade, B. D. Wandelt, I. K. Wehus, M. White, S. D. M. White, A. Wilkinson, D. Yvon, A. Zacchei, and A. Zonca. Planck 2015 results. XIII. Cosmological parameters. *A&A*, 594:A13, September 2016. doi: 10.1051/0004-6361/201525830.

- [59] Joaquin Quinonero-Candela and Carl Edward Rasmussen. A unifying view of sparse approximate Gaussian process regression. *The Journal of Machine Learning Research*, 6:1939–1959, 2005.
- [60] Carl Edward Rasmussen and Christopher K. I. Williams. *Gaussian Processes for Machine Learning*. The MIT Press, second edition, 2006.
- [61] Dongsu Ryu, Hyesung Kang, and Ji-Hoon Ha. A diffusive shock acceleration model for protons in weak quasi-parallel intracluster shocks. <http://arxiv.org/abs/1905.04476v1>, 2019.
- [62] Kevin Schaal and Volker Springel. Shock finding on a moving mesh - I. Shock statistics in non-radiative cosmological simulations. *MNRAS*, 446(4):3992–4007, February 2015. doi: 10.1093/mnras/stu2386.
- [63] Bernhard Schölkopf and Alexander J Smola. *Learning with kernels: support vector machines, regularization, optimization, and beyond*. MIT press, 2018.
- [64] Bernhard Schölkopf, Alexander Smola, and Klaus-Robert Müller. Nonlinear component analysis as a kernel eigenvalue problem. *Neural computation*, 10(5):1299–1319, 1998.
- [65] Leonid Ivanovich Sedov. Propagation of strong shock waves. *Journal of Applied Mathematics and Mechanics*, 10:241–250, January 1946.

[66] Arman Shafieloo, Alex G Kim, and Eric V Linder. Gaussian process cosmography. *Physical Review D*, 85(12):123530, 2012.

[67] Ben Snow, Andrew Hillier, Giulia Murtas, Gert JJ Botha, and Stefano Camera. Shock identification and classification in 2d magnetohydrodynamic compressible turbulence—orszag–tang vortex. *Experimental Results*, 2, 2021.

[68] Rachel S. Somerville and Romeel Davé. Physical Models of Galaxy Formation in a Cosmological Framework. *ARA&A*, 53:51–113, August 2015. doi: 10.1146/annurev-astro-082812-140951.

[69] Volker Springel. The cosmological simulation code GADGET-2. *MNRAS*, 364(4):1105–1134, December 2005. doi: 10.1111/j.1365-2966.2005.09655.x.

[70] Ulrich P. Steinwandel, Benjamin P. Moster, Thorsten Naab, Chia-Yu Hu, and Stefanie Walch. Hot phase generation by supernovae in ISM simulations: resolution, chemistry, and thermal conduction. *MNRAS*, 495(1):1035–1060, June 2020. doi: 10.1093/mnras/staa821.

[71] Ulrich P. Steinwandel, Ludwig M. Boess, Klaus Dolag, and Harald Lesch. On the small scale turbulent dynamo in the intracluster medium: A comparison to dynamo theory. *arXiv e-prints*, art. arXiv:2108.07822, August 2021.

[72] Geoffrey Taylor. The Formation of a Blast Wave by a Very Intense Explosion. I. Theoretical Discussion. *Proceedings of the Royal Society of London Series A*, 201(1065):159–174, March 1950. doi: 10.1098/rspa.1950.0049.

[73] Geoffrey Taylor. The Formation of a Blast Wave by a Very Intense Explosion. II. The Atomic Explosion of 1945. *Proceedings of the Royal Society of London Series A*, 201(1065):175–186, March 1950. doi: 10.1098/rspa.1950.0050.

[74] Rutger van Haasteren and Michele Vallisneri. New advances in the gaussian-process approach to pulsar-timing data analysis. *Physical Review D*, 90(10):104012, 2014.

[75] R. J. van Weeren, F. de Gasperin, H. Akamatsu, M. Brüggen, L. Feretti, H. Kang, A. Stroe, and F. Zandanel. Diffuse radio emission from galaxy clusters. *Space Science Reviews*, 215(1), feb 2019. doi: 10.1007/s11214-019-0584-z.

[76] F. Vazza, K. Dolag, D. Ryu, G. Brunetti, C. Gheller, H. Kang, and C. Pfrommer. A comparison of cosmological codes: properties of thermal gas and shock waves in large-scale structures. *MNRAS*, 418(2):960–985, December 2011. doi: 10.1111/j.1365-2966.2011.19546.x.

[77] F. Vazza, M. Brüggen, D. Wittor, C. Gheller, D. Eckert, and M. Stubbe. Constraining the efficiency of cosmic ray acceleration by cluster shocks. *MNRAS*, 459(1):70–83, June 2016. doi: 10.1093/mnras/stw584.

[78] Stefanie Walch and Thorsten Naab. The energy and momentum input of supernova explosions in structured and ionized molecular clouds. *MNRAS*, 451(3):2757–2771, August 2015. doi: 10.1093/mnras/stv1155.

[79] Cunshi Wang, Yu Bai, C López-Sanjuan, Haibo Yuan, Song Wang, Jifeng Liu, David Sobral, PO Baqui, EL Martín, C Andres Galarza, et al. J-plus: Support vector machine applied to star-galaxy-qso classification. *Astronomy & Astrophysics*, 659:A144, 2022.

[80] Andrew Wilson and Hannes Nickisch. Kernel interpolation for scalable structured gaussian processes (kiss-gp). In *International conference on machine learning*, pages 1775–1784. PMLR, 2015.

[81] Andrew G Wilson, Zhiting Hu, Russ R Salakhutdinov, and Eric P Xing. Stochastic variational deep kernel learning. *Advances in Neural Information Processing Systems*, 29, 2016.

- [82] Andrew Gordon Wilson, Zhiting Hu, Ruslan Salakhutdinov, and Eric P Xing. Deep kernel learning. In *Artificial intelligence and statistics*, pages 370–378. PMLR, 2016.
- [83] Georg Winner, Christoph Pfrommer, Philipp Girichidis, and Rüdiger Pakmor. Evolution of cosmic ray electron spectra in magnetohydrodynamical simulations. *MNRAS*, 488(2):2235–2252, September 2019. doi: 10.1093/mnras/stz1792.
- [84] D. Wittor, F. Vazza, and M. Brüggen. Testing cosmic ray acceleration with radio relics: a high-resolution study using MHD and tracers. *MNRAS*, 464(4):4448–4462, February 2017. doi: 10.1093/mnras/stw2631.
- [85] D. Wittor, F. Vazza, D. Ryu, and H. Kang. Limiting the shock acceleration of cosmic ray protons in the ICM. *MNRAS*, 495(1):L112–L117, June 2020. doi: 10.1093/mnrasl/slaa066.
- [86] Congyao Zhang, Eugene Churazov, Klaus Dolag, William R. Forman, and Irina Zhuravleva. Encounters of merger and accretion shocks in galaxy clusters and their effects on intracluster medium. *MNRAS*, 494(3):4539–4547, May 2020. doi: 10.1093/mnras/staa1013.
- [87] Yanxia Zhang and Yongheng Zhao. Automated clustering algorithms for classification of astronomical objects. *Astronomy & Astrophysics*, 422(3):1113–1121, 2004.

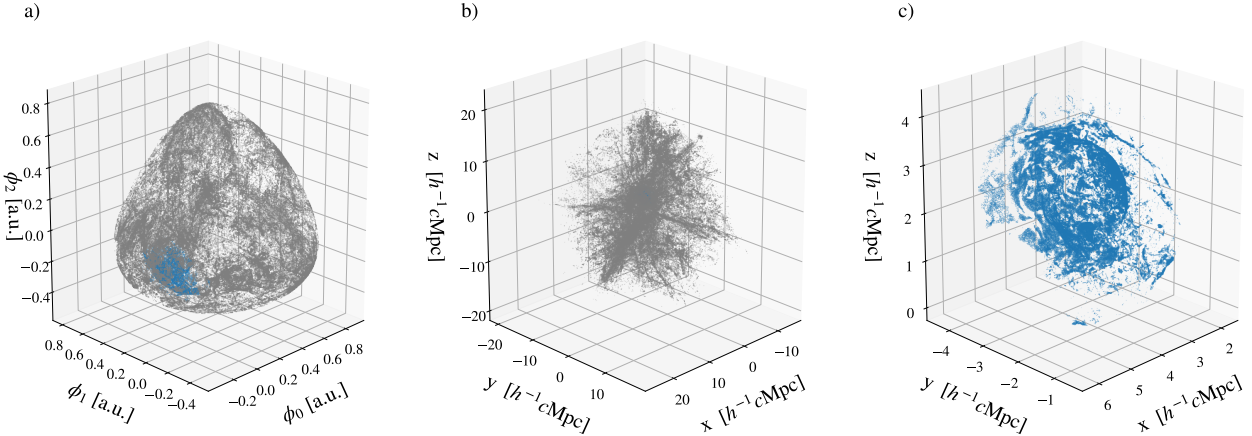


Figure A.7: VIRGO result - Denoising process for CLUSTHD₁ data set. *a)* GMM fitted in kernel-PCA space with low-density noise component (gray) and high-density cluster component (blue). *b)* Labeled data from *a*), but shown in physical space. *c)* Resulting denoised data set.

Appendix A. Appendix

This section provides additional plots to visualize further and underline the results and claims in Sec. 5. Furthermore, we hope to clarify the visual verification of results. We present and discuss more results with VIRGO as well as other attempts with other approaches to highlight the difficulty of the problem and distinct performance of VIRGO. For the latter section, we will only focus on the single cluster data set CLUSTHD₃, as more complex cases are far out of reach for other approaches. All VIRGO results are determined with the fully automatic pipeline for all data sets without fine-tuning.

All assets, code, and data sets are cited and credited in the main paper. We did not want to expand the main document with a large appendix for the submission and instead made an extensive supplementary document.

Appendix A.1. VIRGO - Denoising and Centering

We show the denoising process of Sec. 4 step 2) from Fig. 3 and its impact on the remaining data sets. The GMM is fitted in kernel-PCA space with low-density noise and high-density cluster component. We only plot the first three kernel space dimensions and show the removal of non-shock wave particles before and after.

The Fig. A.7 - A.9 show how VIRGO ideally separates and centers on the cluster of shock waves from the enveloping cloud of non-shock wave particles.

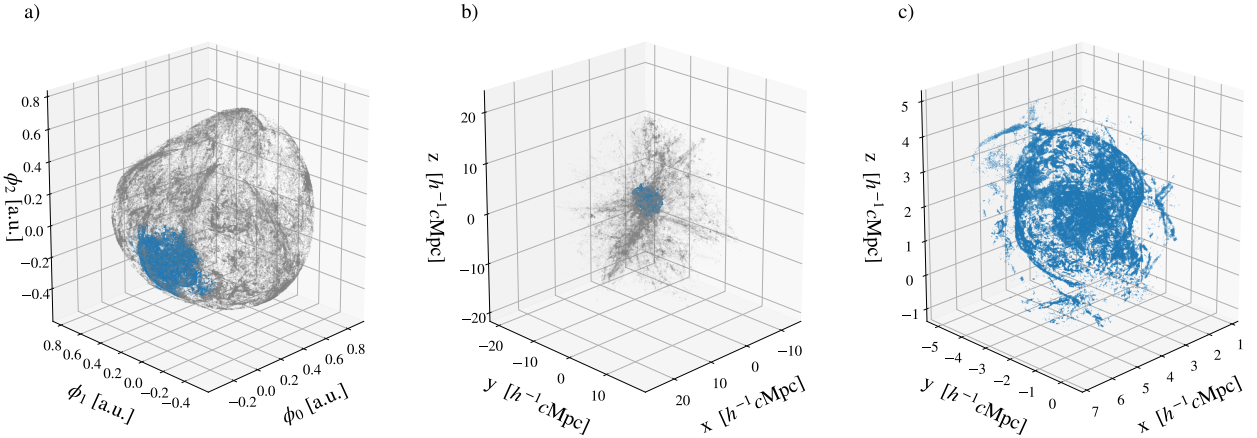


Figure A.8: VIRGO result - Denoising process for CLUSTHD₃ data set. *a)* GMM fitted in kernel-PCA space with low-density noise component (gray) and high-density cluster component (blue). *b)* Labeled data from *a*), but shown in physical space. *c)* Resulting denoised data set.

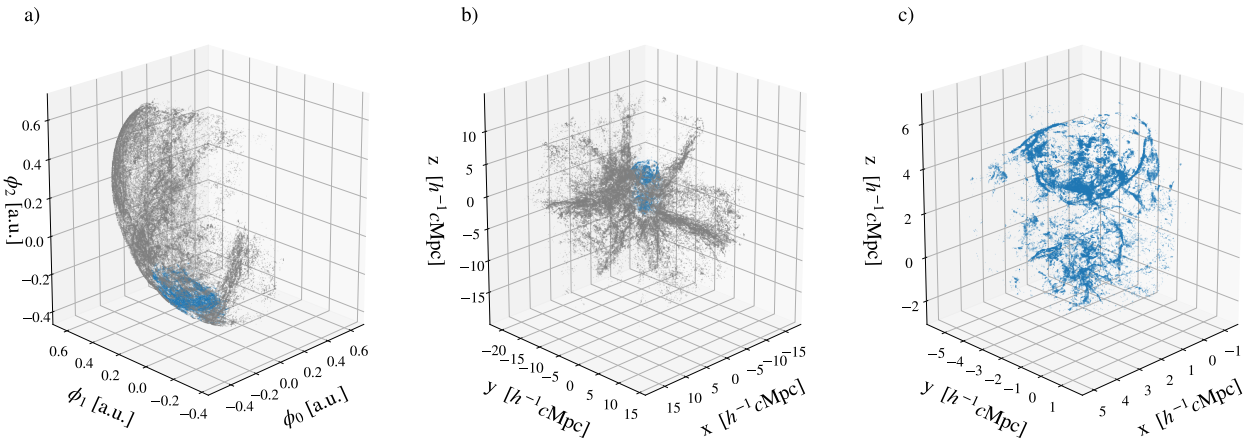


Figure A.9: VIRGO result - Denoising process for CLUSTMHD₁ data set. *a)* GMM fitted in kernel-PCA space with low-density noise component (gray) and high-density cluster component (blue). *b)* Labeled data from *a*), but shown in physical space. *c)* Resulting denoised data set.

Appendix A.2. VIRGO - Classification of Subset

Similar to Fig. 4, we show the classification result of the denoised subsets of all data sets as well as an additional cluster from BoxMHD, BoxMHD₂. Each result is plotted for six different angles, once with and without classified non-shock wave particles. The clear separation of the shock wave surfaces from non-shock wave particles is clearly visible, and the general quality of the classification in terms of coherent shock wave surfaces is verifiable. In addition, the estimated error of labeling shock surface particles as non-shock wave particles is visibly negligible.

Fig. A.10 shows an almost ideal result. There are some non-shock wave particles above the smallest shock wave (green). The other two shock waves (blue, orange) are ideal. Fig. A.11 additionally shows the classified non-shock wave particles, and smaller structures remain. We consciously ignore such structures with a minimum class size parameter (VIRGO hyperparameter). Fig. A.12 - Fig. A.15 show ideal results. Fig. A.16 shows how the most relevant and largest shock wave (blue) is ideally separated and classified. However, smaller structures (all other colors) are hard to determine as shock wave structures, as they could also be a cluster of even smaller structures. This differentiation and focus on larger structures when shock wave sizes vary is a limitation of VIRGO. A criterion whether VIRGO found a shock wave surface, as we discussed in Sec. 6, would help to solve this problem for future work. Fig. A.18 shows generally very good results. However, a thin structure (brown) is misclassified and should belong to the primary shock wave (blue). All other shock wave structures are correctly separated and classified. Fig. A.20 and Fig. A.21 show the classification of very small structures in a faint cloud of non-shock wave particles. A few non-shock wave particles are misclassified as part of the shock wave structures.

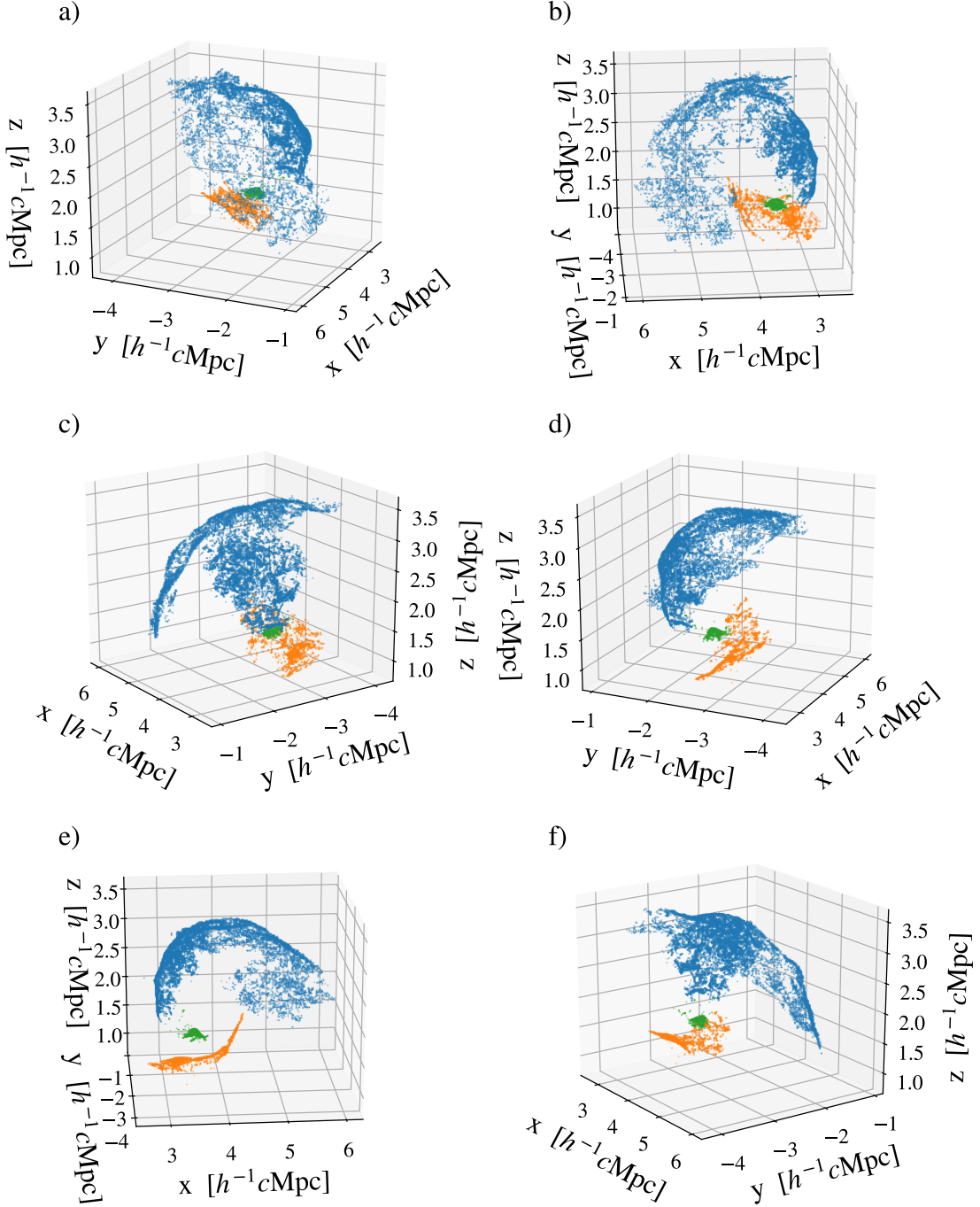


Figure A.10: VIRGO result - We show the labeled subset of CLUSTHD₁ after the denoising process. The classification is done as described in Sec. 4 step 3). *a) - f)* Full rotation in 60° steps.

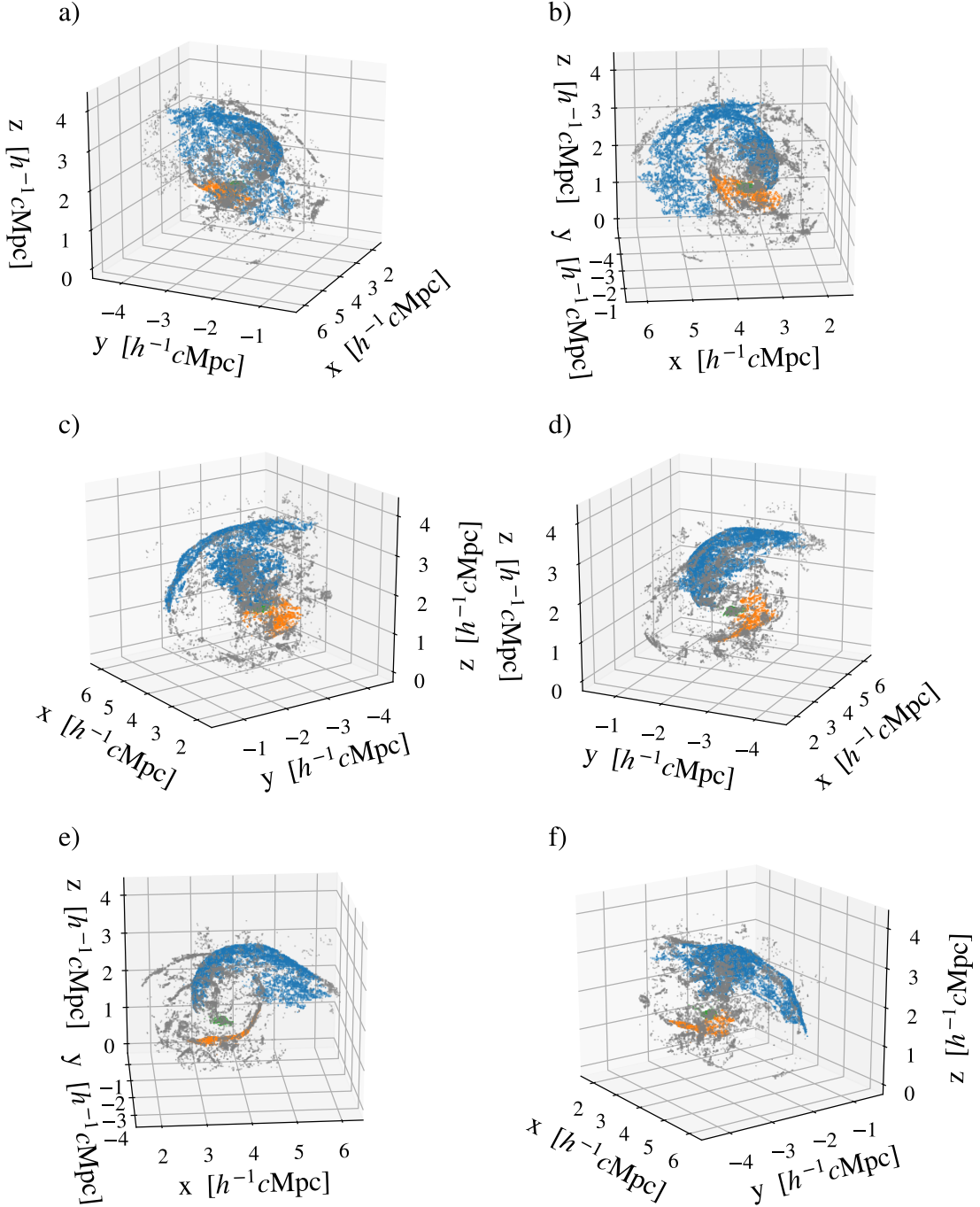


Figure A.11: VIRGO result - We show the labeled subset of CLUSTHD₁ after the denoising process. The classification is done as described in Sec. 4 step 3) and non-shock wave particles are plotted too. a) - f) Full rotation in 60° steps.

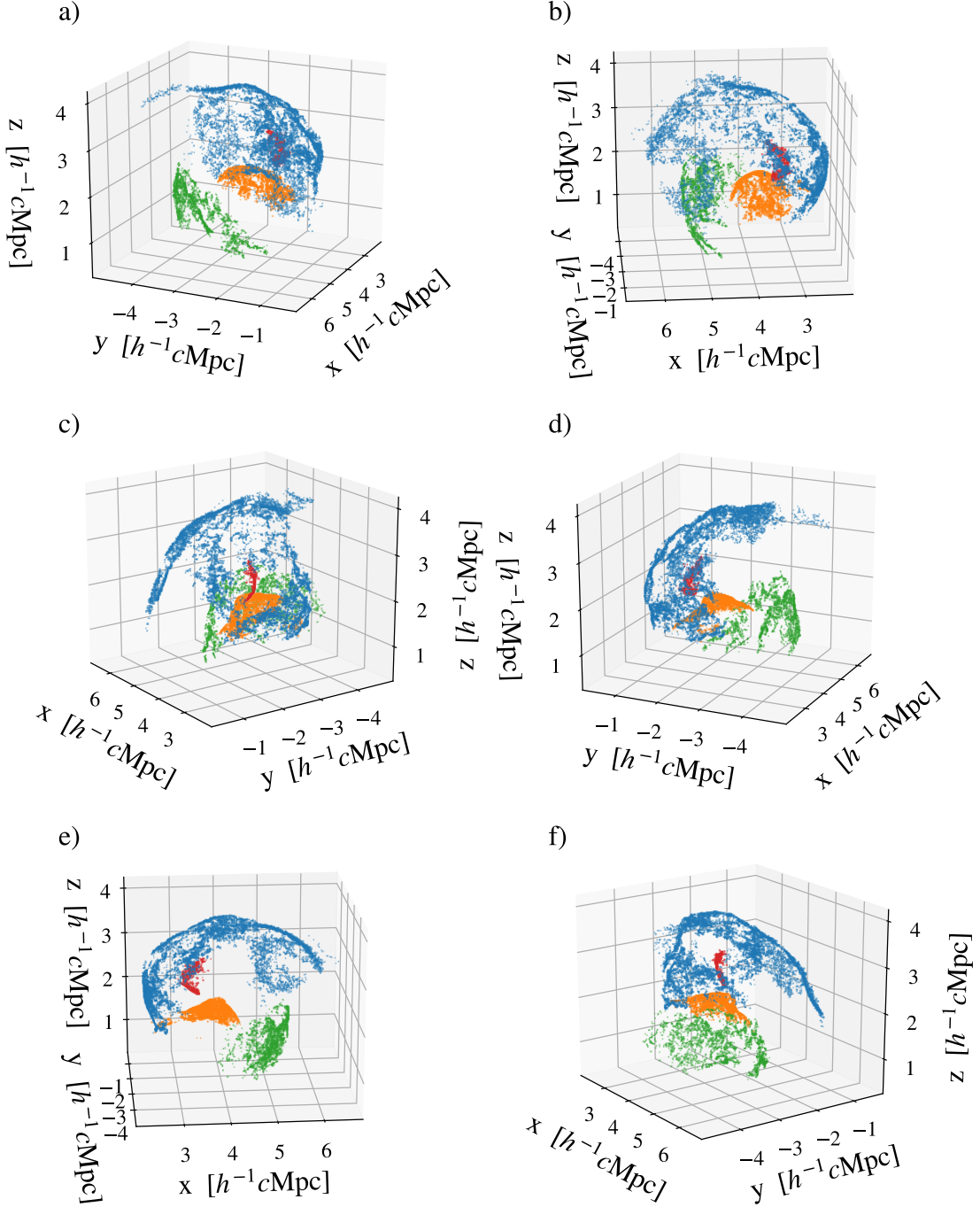


Figure A.12: VIRGO result - We show the labeled subset of CLUSTHD₂ after the denoising process. The classification is done as described in Sec. 4 step 3). a) - f) Full rotation in 60° steps.

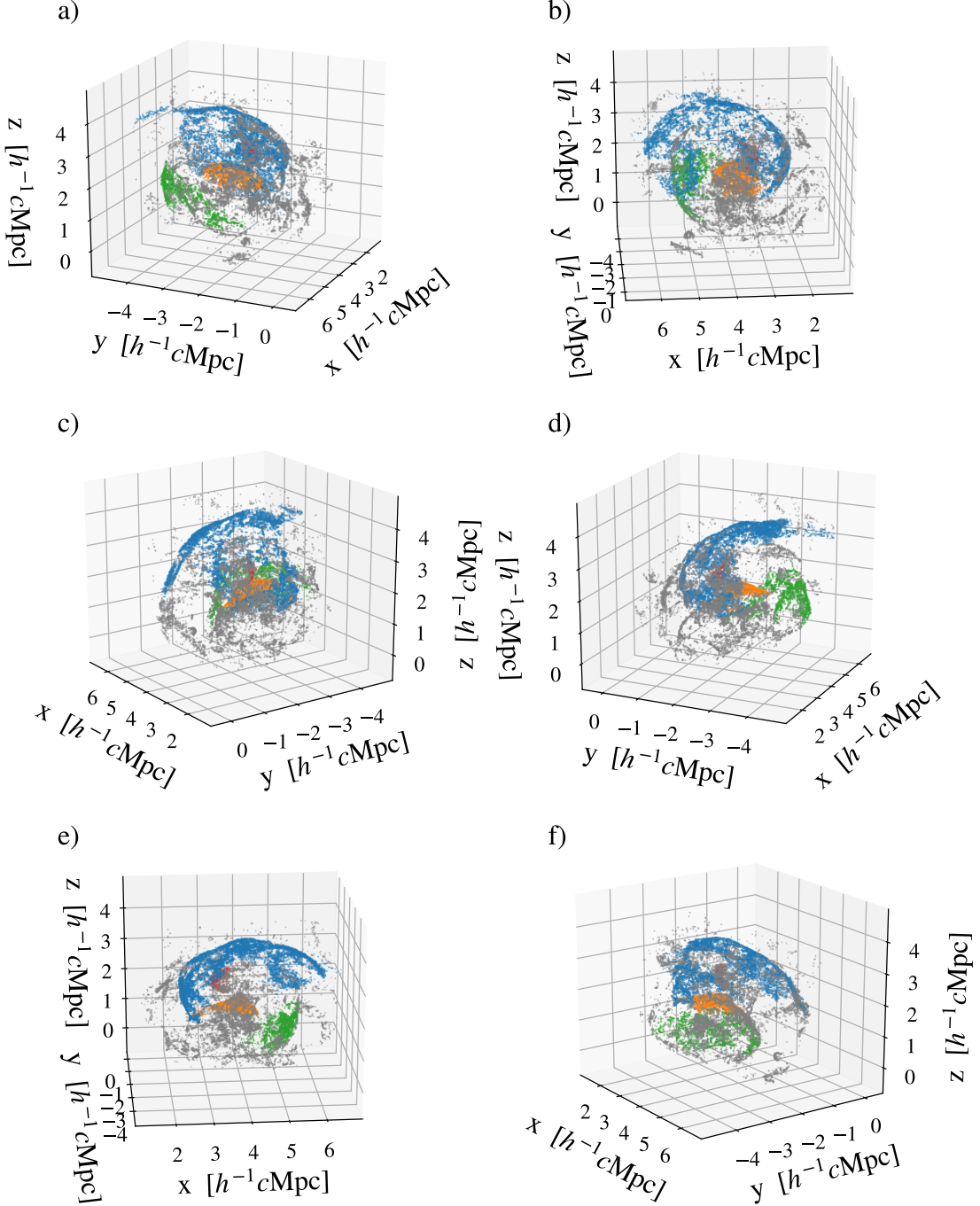


Figure A.13: VIRGO result - We show the labeled subset of CLUSTHD₂ after the denoising process. The classification is done as described in Sec. 4 step 3) and non-shock wave particles are plotted too. a) - f) Full rotation in 60° steps.

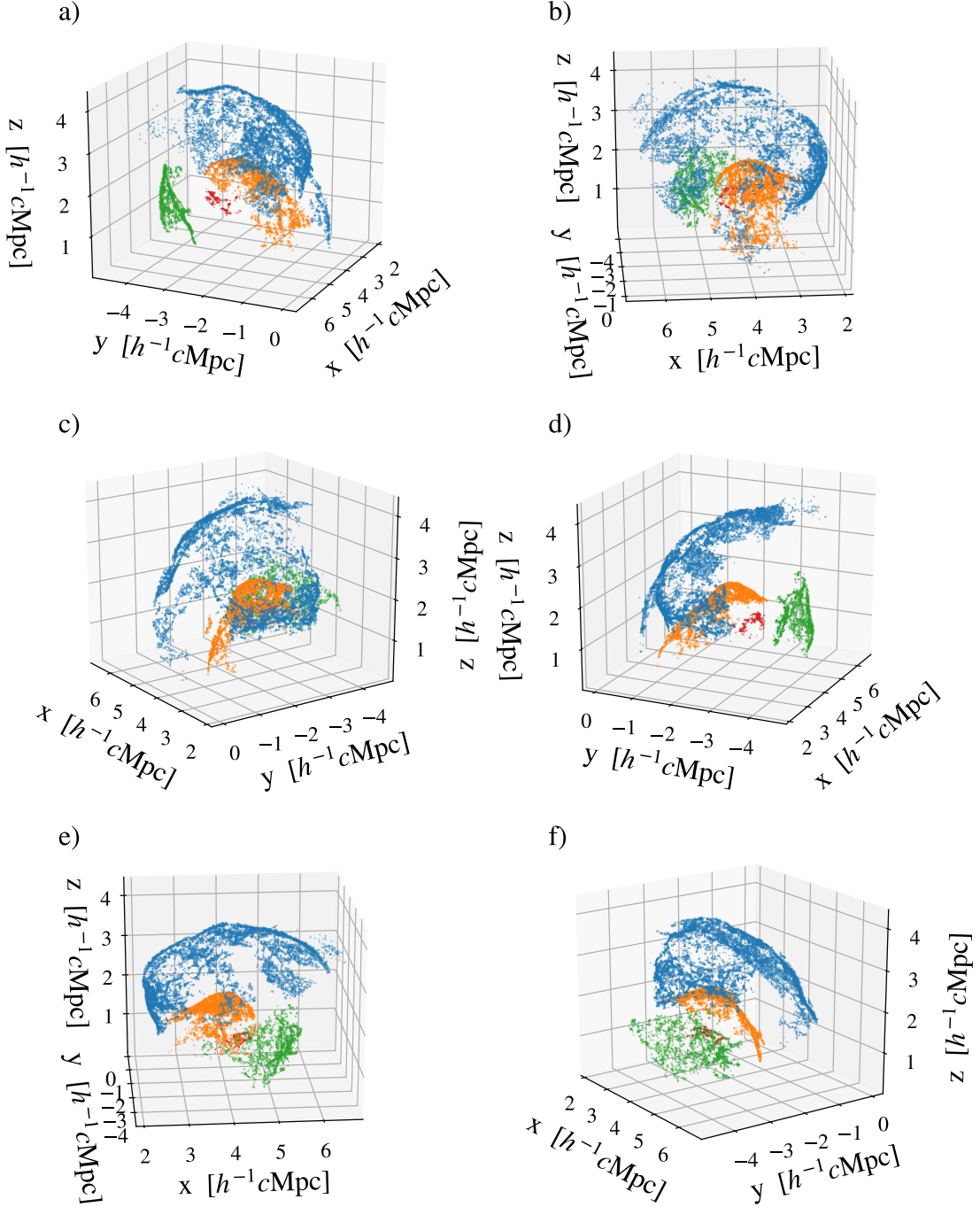


Figure A.14: VIRGO result - We show the labeled subset of CLUSTHD₃ after the denoising process. The classification is done as described in Sec. 4 step 3). a) - f) Full rotation in 60° steps.

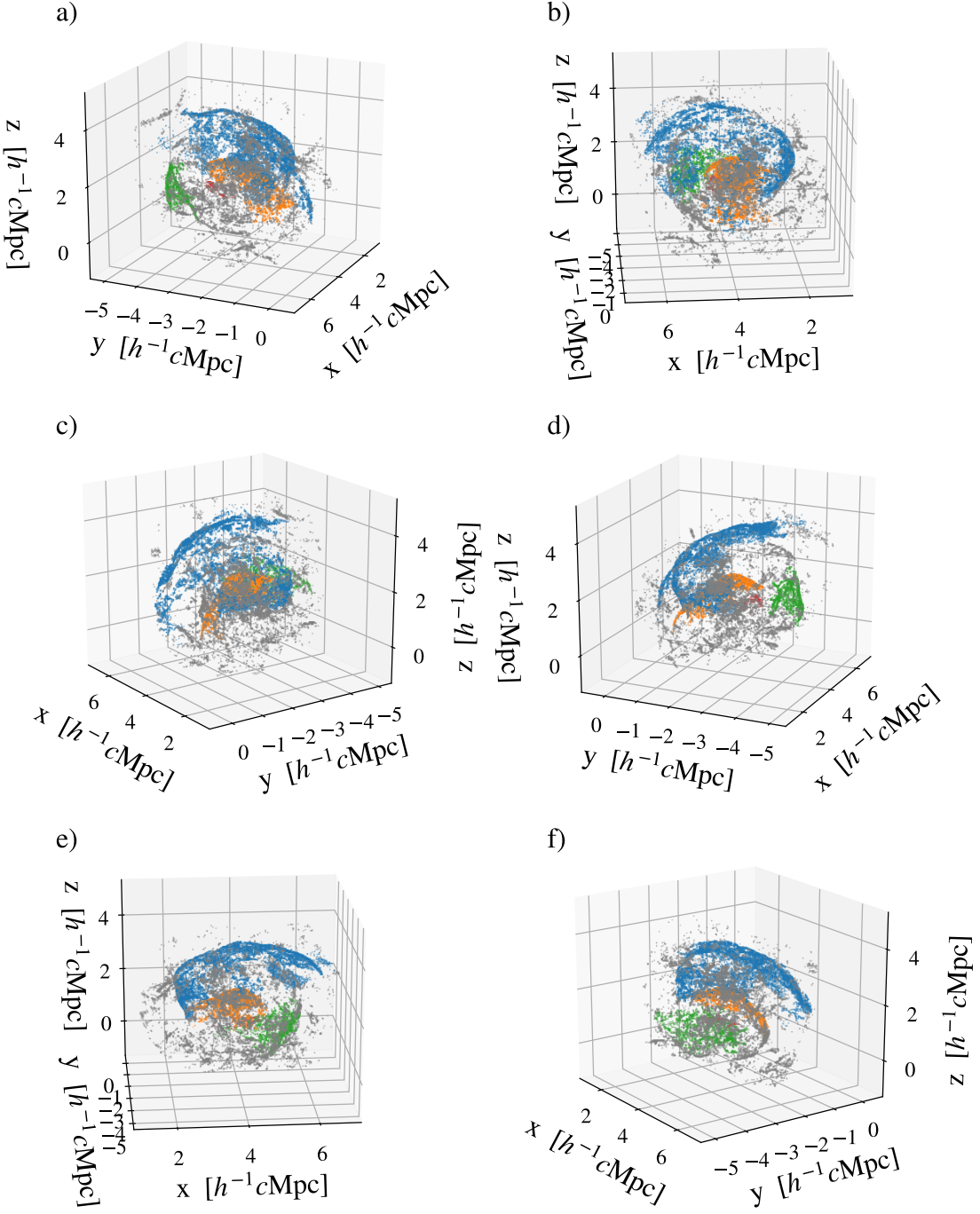


Figure A.15: VIRGO result - We show the labeled subset of CLUSTHD₃ after the denoising process. The classification is done as described in Sec. 4 step 3) and non-shock wave particles are plotted too. a) - f) Full rotation in 60° steps.

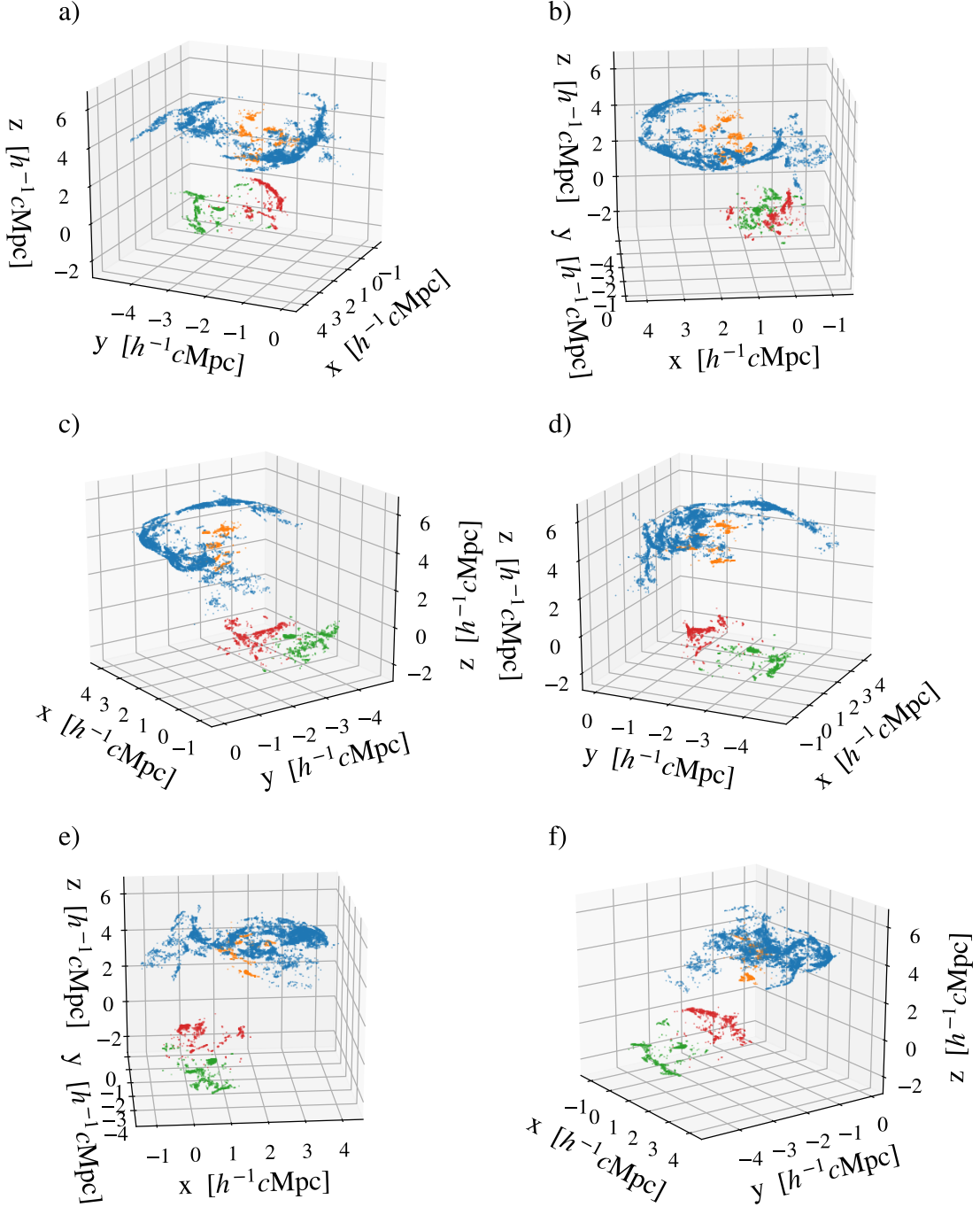


Figure A.16: VIRGO result - We show the labeled subset of CLUSTMHD₁ after the denoising process. The classification is done as described in Sec. 4 step 3). a) - f) Full rotation in 60° steps.

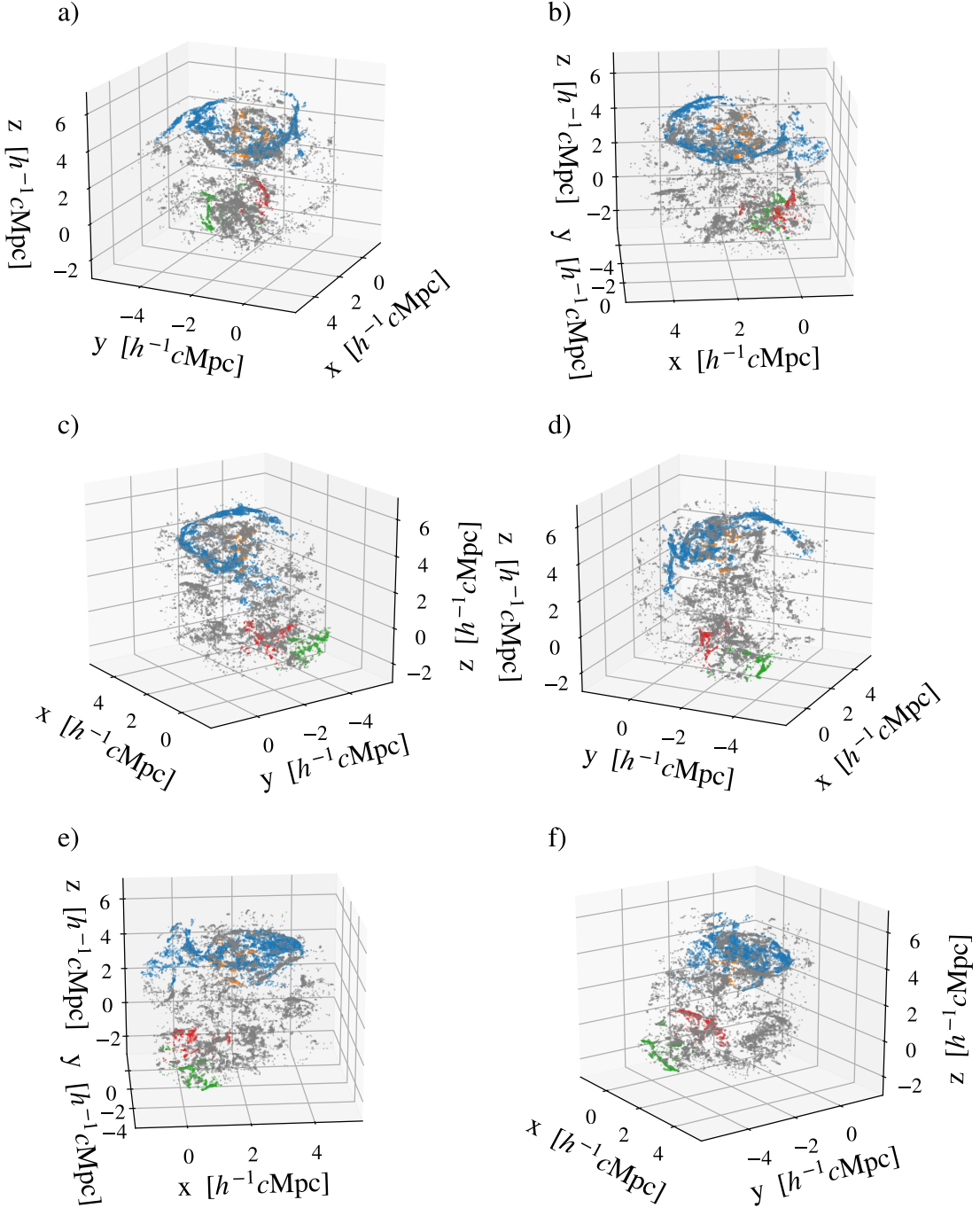


Figure A.17: VIRGO result - We show the labeled subset of CLUSTMHD_1 after the denoising process. The classification is done as described in Sec. 4 step 3) and non-shock wave particles are plotted too. a) - f) Full rotation in 60° steps.

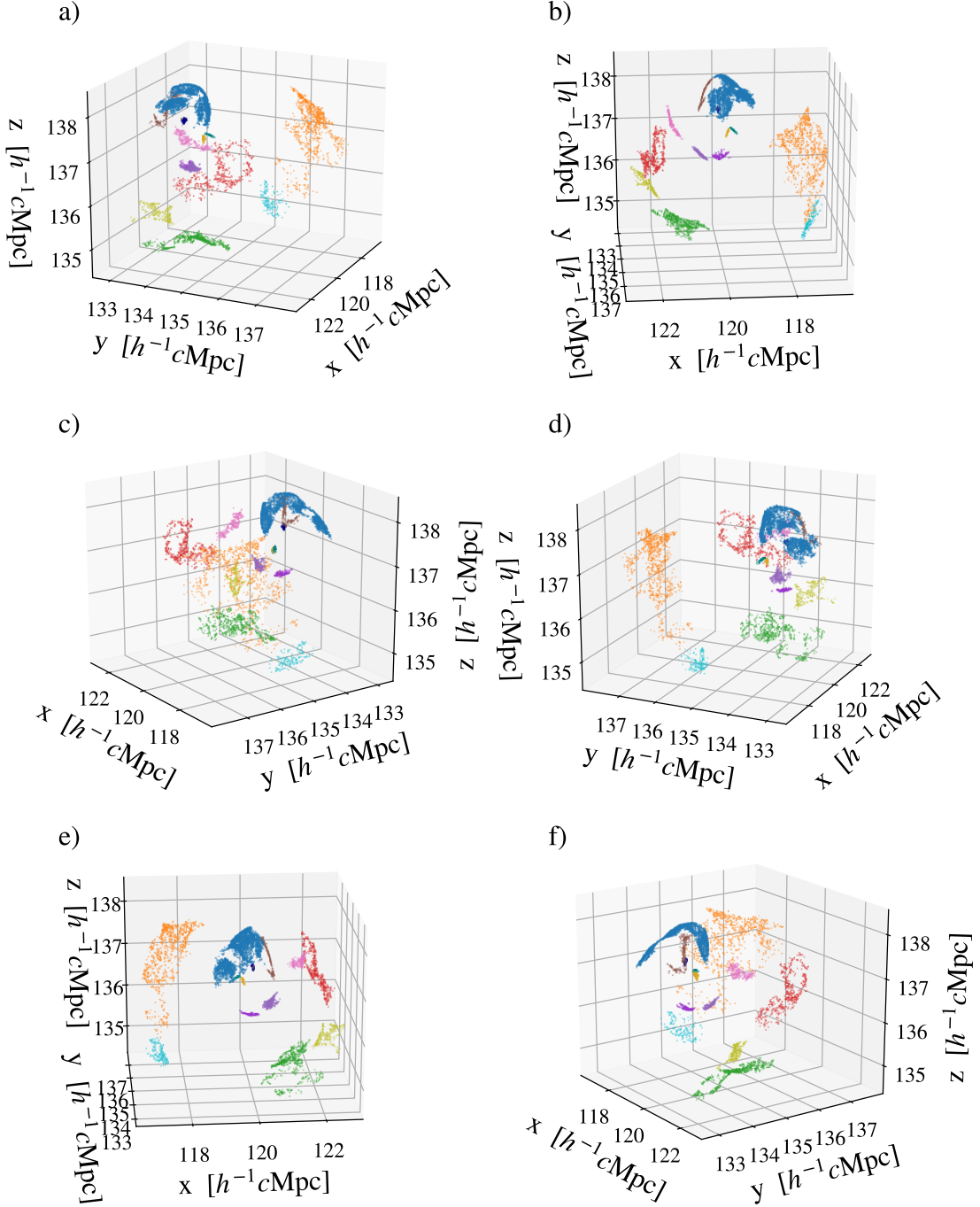


Figure A.18: VIRGO result - We show the labeled subset of BoxMHD₁ after the denoising process. The classification is done as described in Sec. 4 step 3). a) - f) Full rotation in 60° steps.

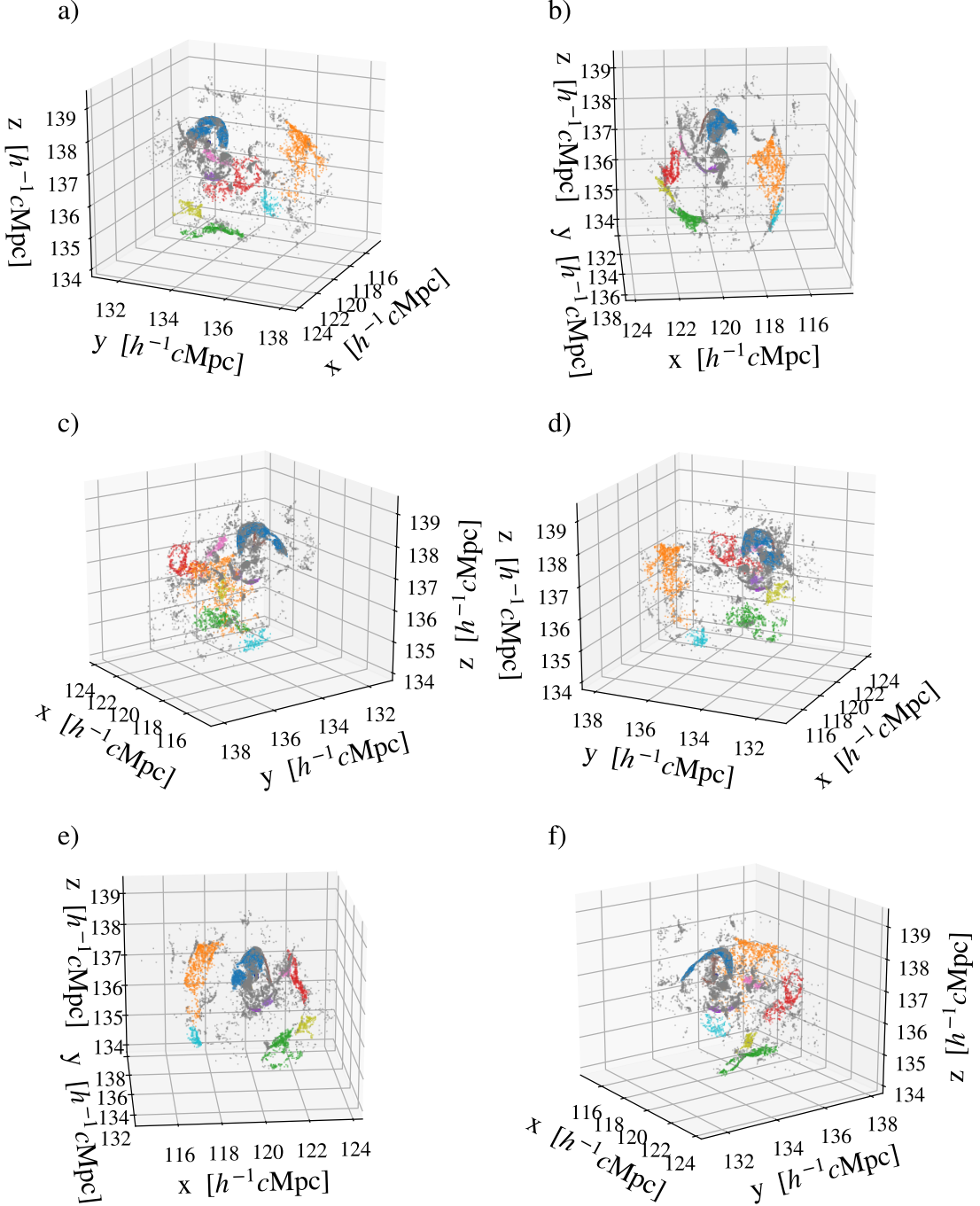


Figure A.19: VIRGO result - We show the labeled subset of BoxMHD₁ after the denoising process. The classification is done as described in Sec. 4 step 3) and non-shock wave particles are plotted too. a) - f) Full rotation in 60° steps.

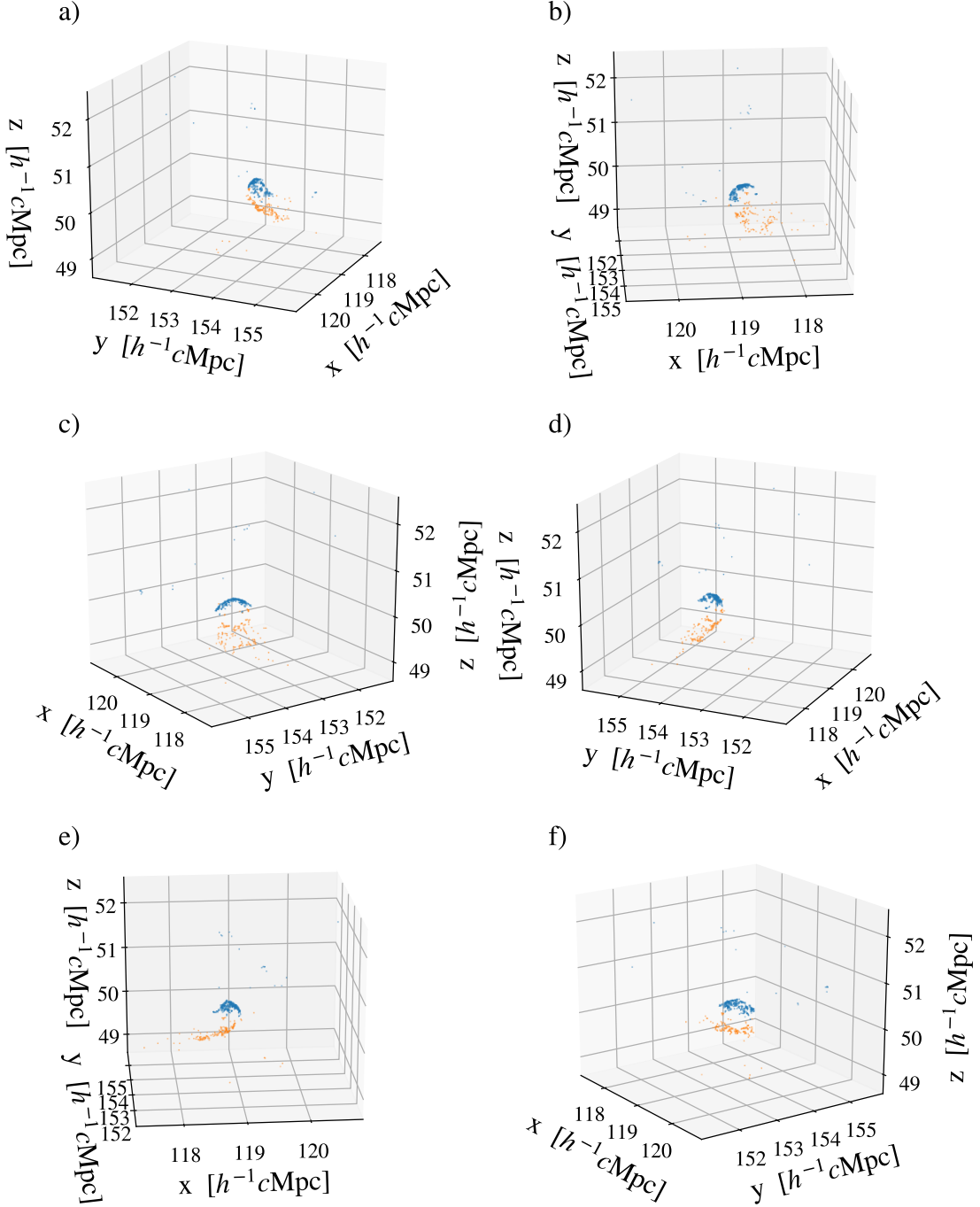


Figure A.20: VIRGO result - We show the labeled subset of BoxMHD₁ after the denoising process. The classification is done as described in Sec. 4 step 3). a) - f) Full rotation in 60° steps.

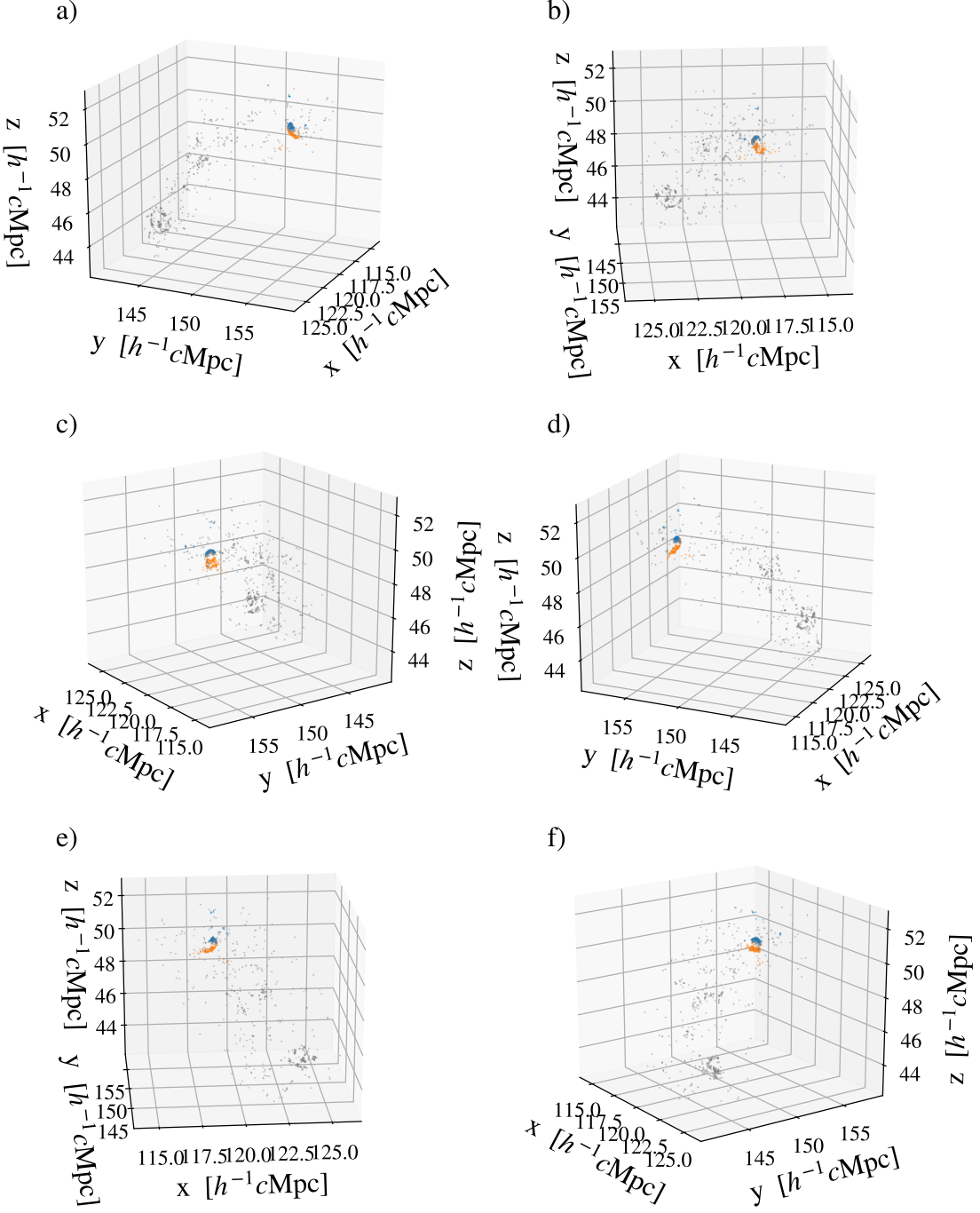


Figure A.21: VIRGO result - We show the labeled subset of BoxMHD₁ after the denoising process. The classification is done as described in Sec. 4 step 3) and non-shock wave particles are plotted too. a) - f) Full rotation in 60° steps.

Appendix A.3. VIRGO - SV-DKL Resolution Reconstruction

Similar to Fig. 5, we show the full resolution reconstruction with the SV-DKL classifier. We trained it on the labeled subset from step 3) for each data set separately. Each result is plotted for six different angles without classified non-shock wave particles due to illustrative purposes. These results are the final VIRGO outputs for the raw inputs and allow scalability to large data sets. The separation of the shock wave surfaces from non-shock wave particles is clearly visible, and the general quality of the classification in terms of coherent shock wave surfaces is verifiable.

Fig. A.22 shows an ideal result for the large shock wave surface (blue). The smaller shock waves (orange, green) are contaminated with a few non-shock wave particles, especially the smallest one (green). The contamination is a propagated error from the previous labeling step and can be seen to some extent in Fig. A.10. Fig. 5 shows ideal results for the smaller shock wave structures (green, orange, red), but some contaminating non-shock wave particles on top of the large shock wave surface (blue). This issue is caused by too aggressive denoising in step 2) as this leads to too little data in the labeled subset above the large shock surface to robustly classify the relevant particles. Fig. A.23 presents an ideal result with VIRGO. All shock wave surfaces are correctly separated and classified. The SV-DKL classified all non-shock wave particles correctly as irrelevant. Fig. A.24 shows a correct separation and classification of the large shock wave with a complex shape (blue). However, smaller structures (all other colors) are hard to determine as shock wave structures, as they could also be a cluster of even smaller structures. This differentiation and focus on larger structures when shock wave sizes vary is a limitation of VIRGO. A criterion whether VIRGO found a shock wave surface, as we discussed in Sec. 6, would help to solve this problem for future work.

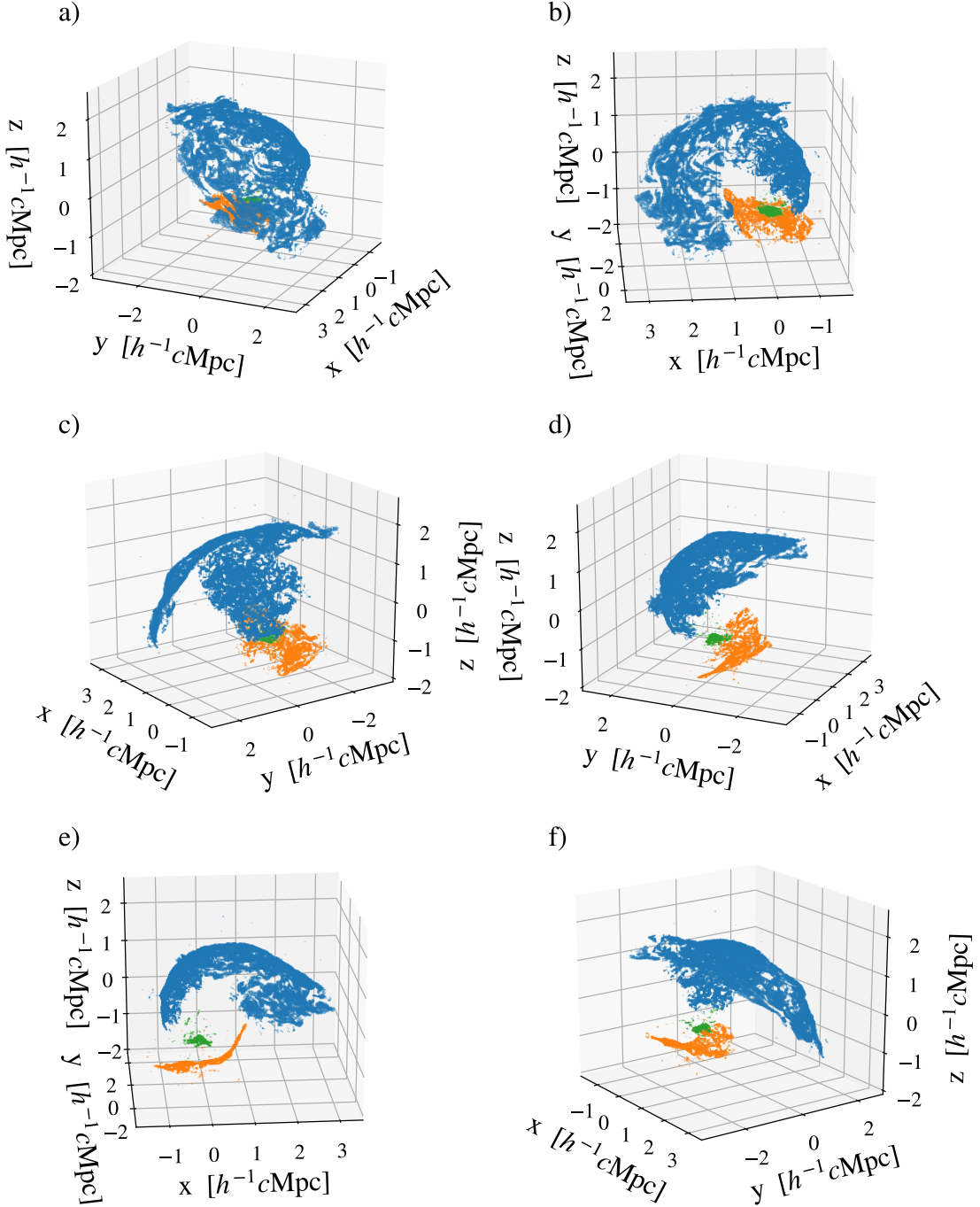


Figure A.22: VIRGO result - We show the full resolution reconstruction of $CLUSTHD_1$ after the denoising and subset labeling process. The classification is done as described in Sec. 4 step 4) with SV-DKL. a) - f) Full rotation in 60° steps.

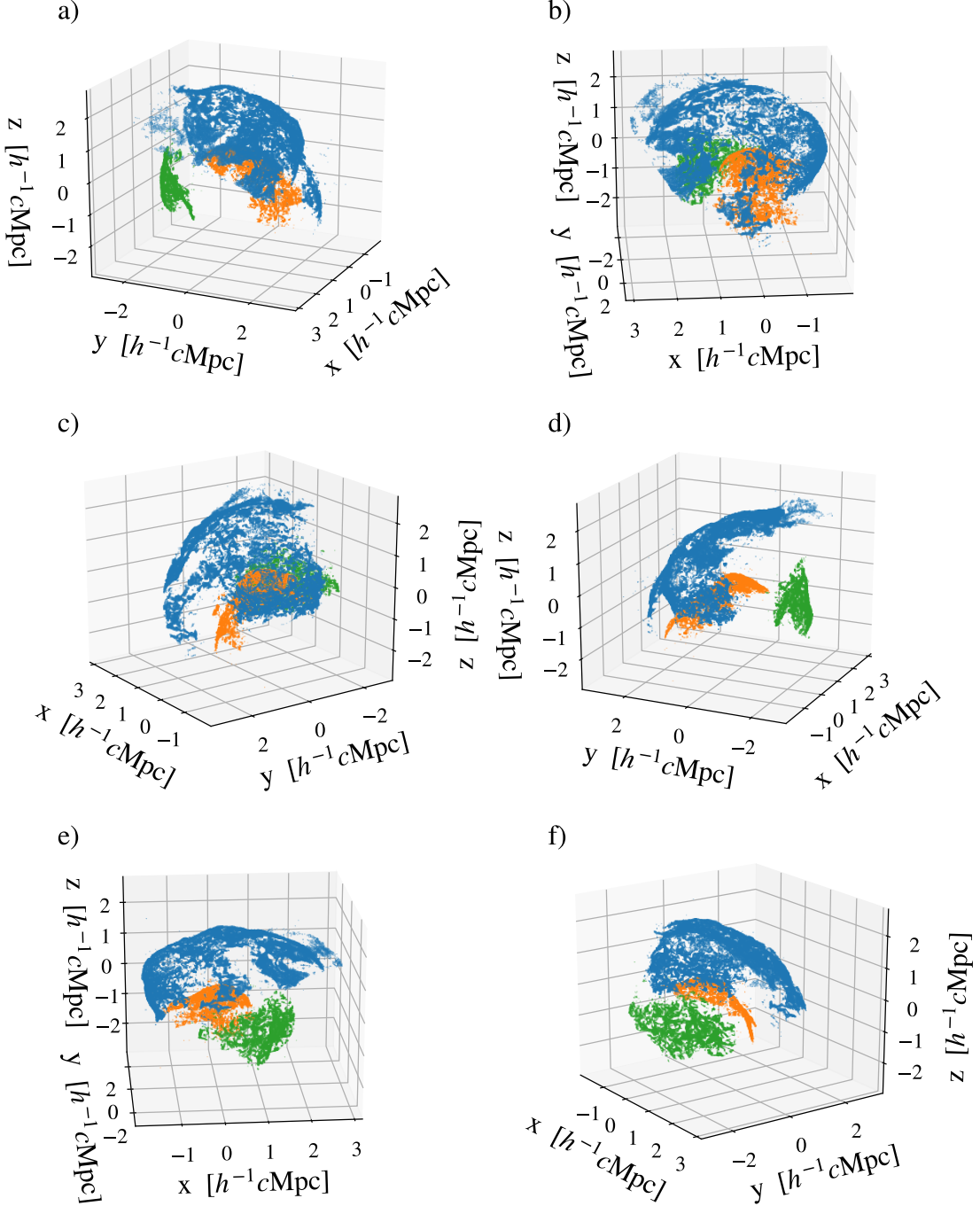


Figure A.23: VIRGO result - We show the full resolution reconstruction of CLUSTHD₃ after the denoising and subset labeling process. The classification is done as described in Sec. 4 step 4) with SV-DKL. *a) - f)* Full rotation in 60° steps.

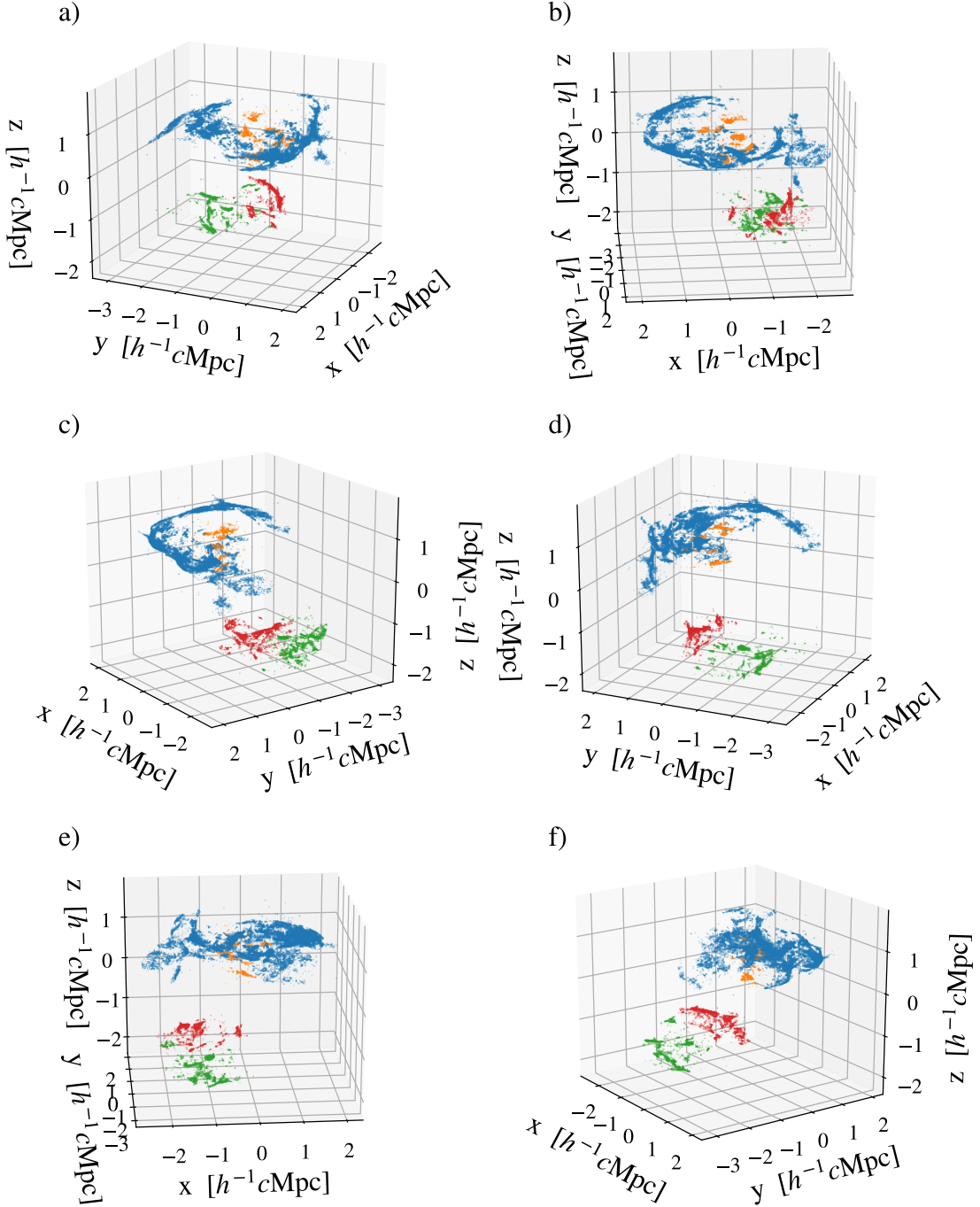


Figure A.24: VIRGO result - We show the full resolution reconstruction of CLUSTMHD₁ after the denoising and subset labeling process. The classification is done as described in Sec. 4 step 4) with SV-DKL. a) - f) Full rotation in 60° steps.

Appendix A.4. VIRGO - SV-DKL Generalization Tests

We claimed in Sec. 5 that the SV-DKL generalizes over different data sets, as long as the number of target classes is the same. We tested the generalization on the CLUSTHD data set by training the SV-DK on the labeled subset of time step CLUSTHD₂. We show the achieved full resolution reconstructions of CLUSTHD₃, CLUSTHD₄ and CLUSTHD₅, which are all later time steps of the same simulation. Different time steps mean changing shapes and shock wave propagation from one data set to another.

As can be seen in the Fig. A.25 - A.27, VIRGO provides good resolution reconstruction over different data sets, even though shock wave positions, surface densities and sizes change. There is little to no contaminating noise on the results.

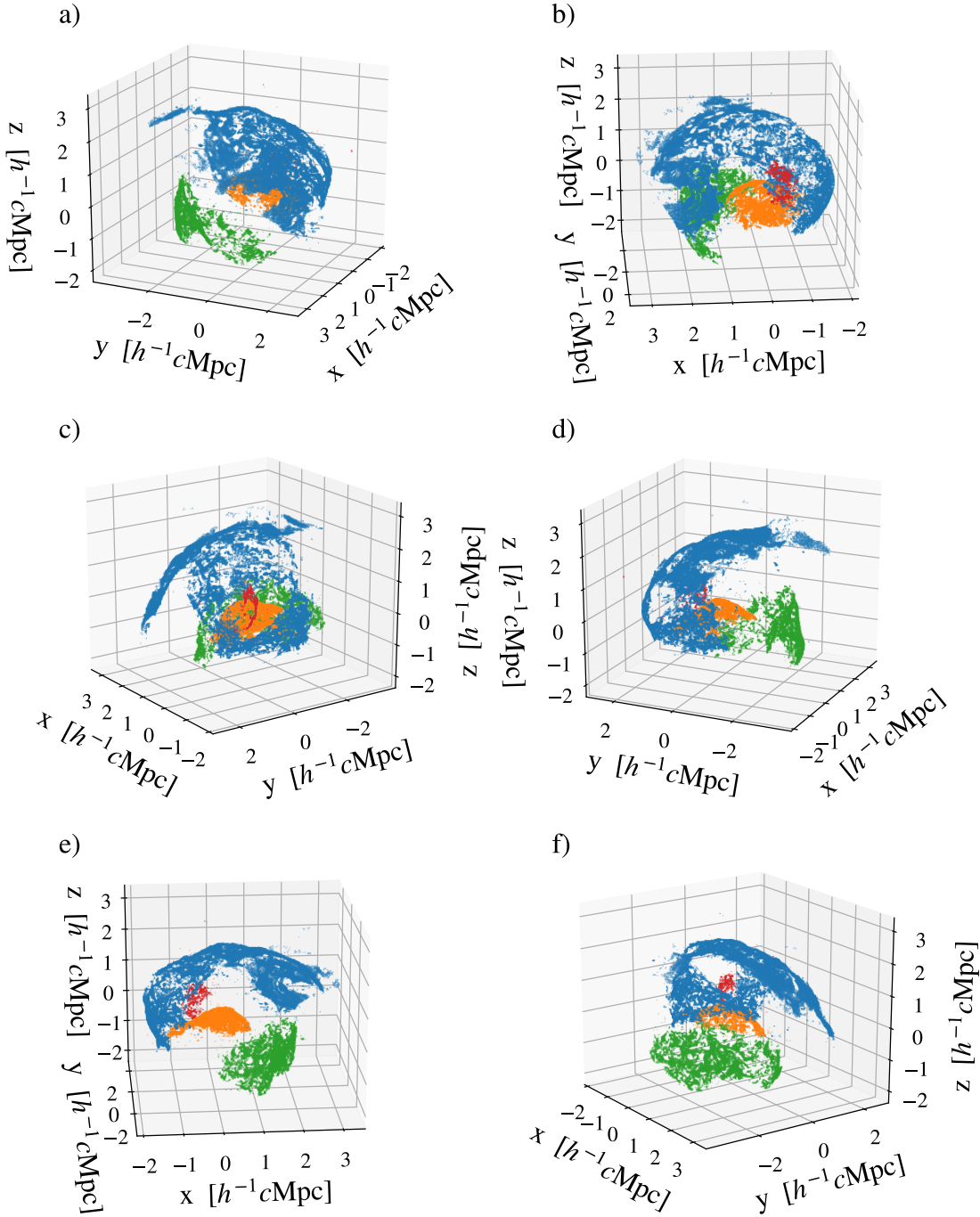


Figure A.25: VIRGO result - We show the generalization on the full resolution reconstruction of CLUSTHD₃. a) - f) Full rotation in 60° steps.

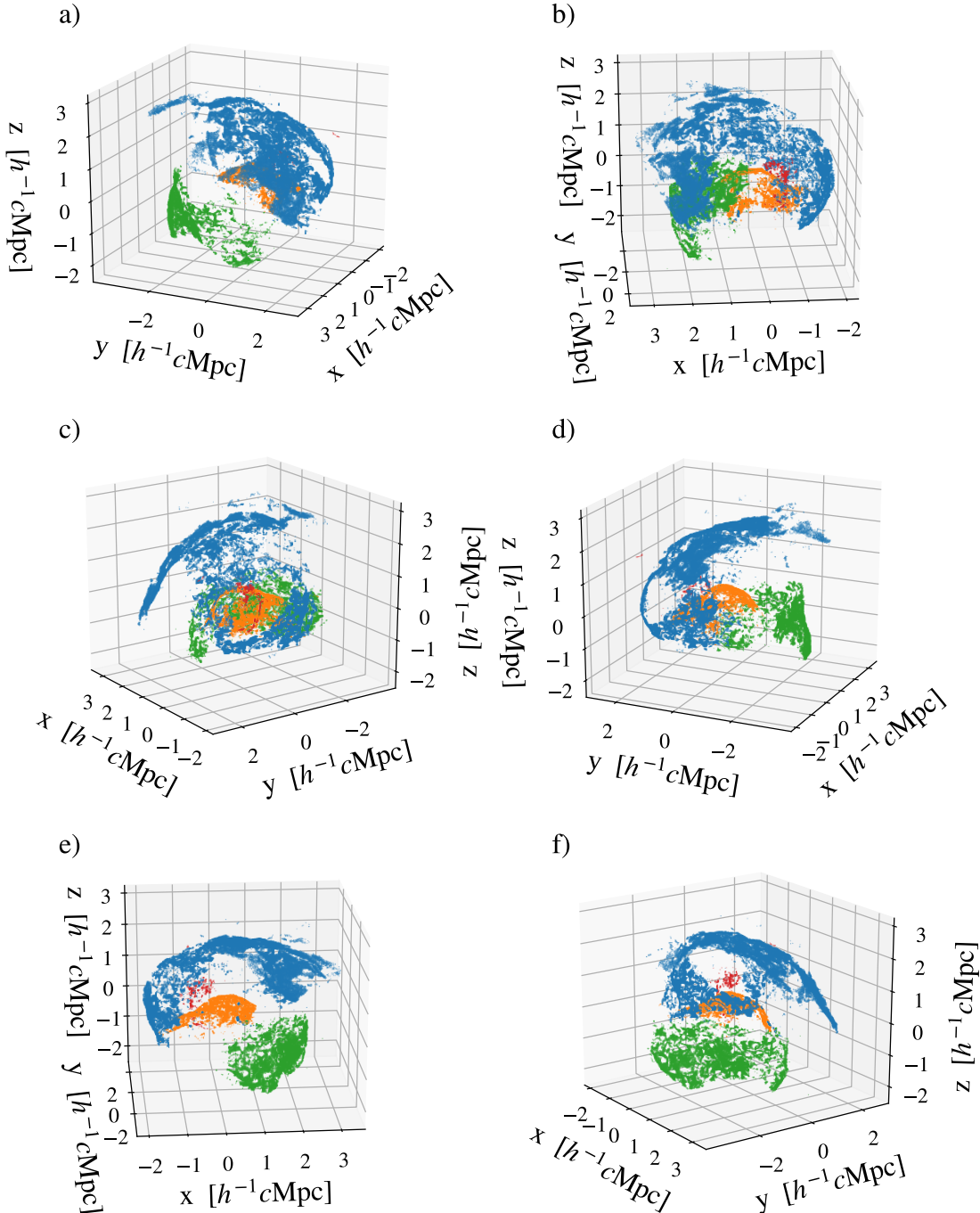


Figure A.26: VIRGO result - We show the generalization on the full resolution reconstruction of CLUSTHD₄. a) - f) Full rotation in 60° steps.

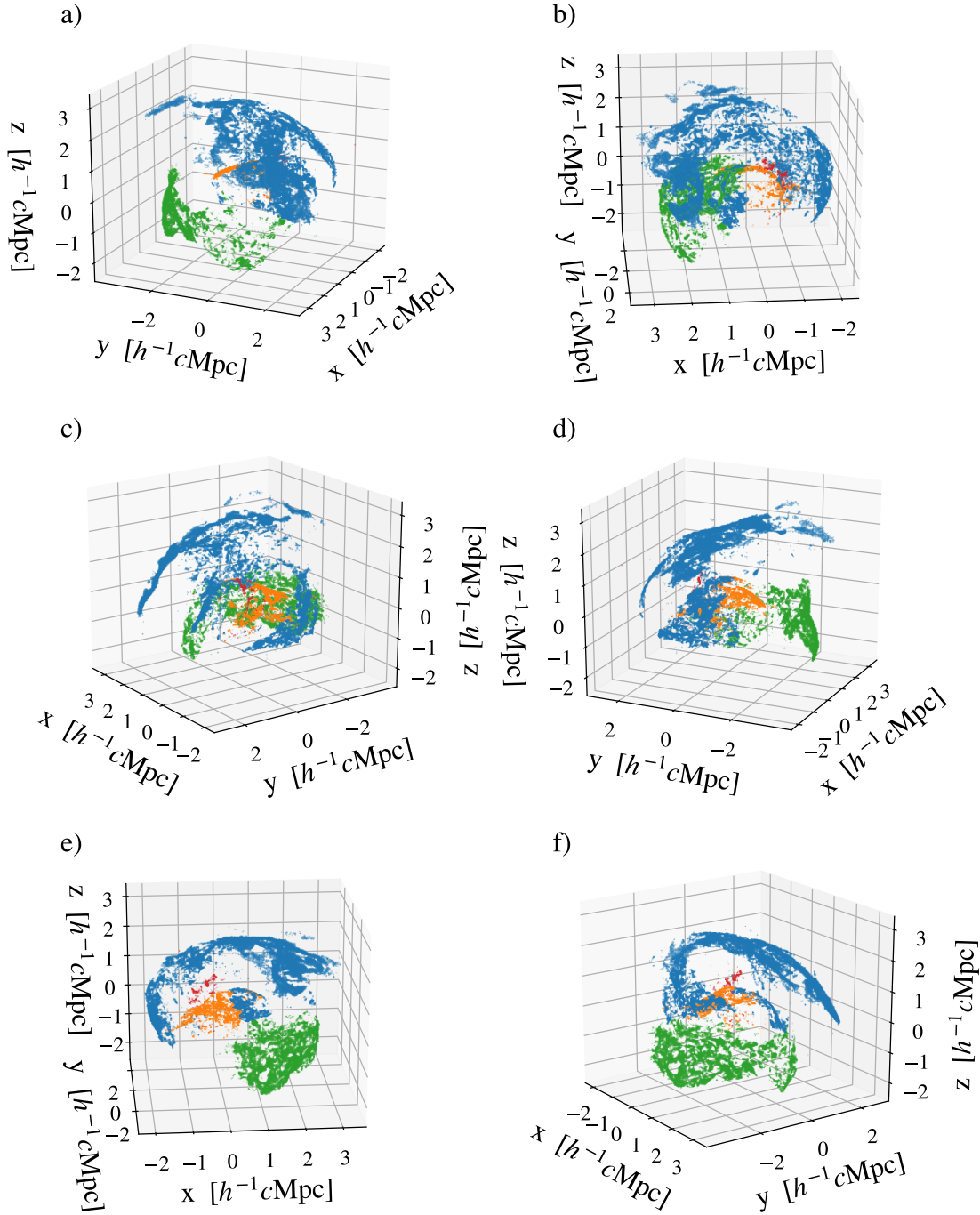


Figure A.27: VIRGO result - We show the generalization on the full resolution reconstruction of CLUSTHD₅. a) - f) Full rotation in 60° steps.

Appendix A.5. Other approaches

We present and discuss attempts with other approaches to highlight the difficulty of the problem and the distinct performance of VIRGO. For this section, we will only focus on the single cluster data set CLUSTHD₃, as more complex cases are far out of reach for other approaches. Unlike with VIRGO in previous sections, we manually fine-tune all results in this section to achieve the best possible results. The used approaches are outlined and referenced in Sec. 2.

Fig. A.28 shows the application of a FoF algorithm with a fixed linking length on the full, raw data set. Due to the high number of non-shock wave particles on the raw data set, any automatic linking length estimation fails, and we need to tune it manually ($\beta = 0.045$). This result motivated the VIRGO project. There are problems while the full spatial resolution is intact and the shock wave objects are separated and classified. The most significant shock wave (blue) has non-shock wave particles close above its surface, and another, separate structure clearly does not belong to the shock wave (Fig. A.28b right, Fig. A.28e left, Fig. A.28f left). Furthermore, the central shock wave structure (orange) has a separate structure not belonging to it wrongly classified (Fig. A.28c bottom left, Fig. A.28f bottom right). Furthermore, the central shock wave structure (orange) is highly contaminated with non-shock wave particles above and even more so below its curved surface. This problem is hard to illustrate with limited print capabilities, but it can be seen in the less dense following plots with similar issues. The lack of automation as well as high contamination set the requirements for a solution such as VIRGO. Fig. A.29 shows the application of a FoF algorithm with a fixed linking length on the denoised data set. The linking length was manually tuned ($\beta = 0.090$). Apart from strong non-shock wave particle contamination, it is impossible to successfully combine the two large shock waves (orange, green) without including the central structure (blue). Any result with this approach is not scientifically usable. Any of the following results would need a scalability solution, such as SV-DKL, to reconstruct the full spatial resolution, as the data sets need to be reduced due to the hardware requirements of DBSCAN. Fig. A.30 shows the application of DBSCAN on particle positions of the raw data set. We manually set the distance parameter to $\epsilon = 0.025$ with a minimum density group size of 15. Following previous points, even with manual tuning, any results with this approach are not scientifically usable. Fig. A.31 shows the application of DBSCAN on particle positions and norm vectors of the raw data set. We manually set the distance parameter to $\epsilon = 0.14$ with a minimum density group size of 15. Following previous points, even with manual tuning, any results with this approach are not scientifically usable. Fig. A.32 shows the application of DBSCAN on the denoised data set. We manually set the distance parameter to $\epsilon = 0.11$ with a minimum density group size of 15. Following previous points, even with manual tuning, any results with this approach are not scientifically usable.

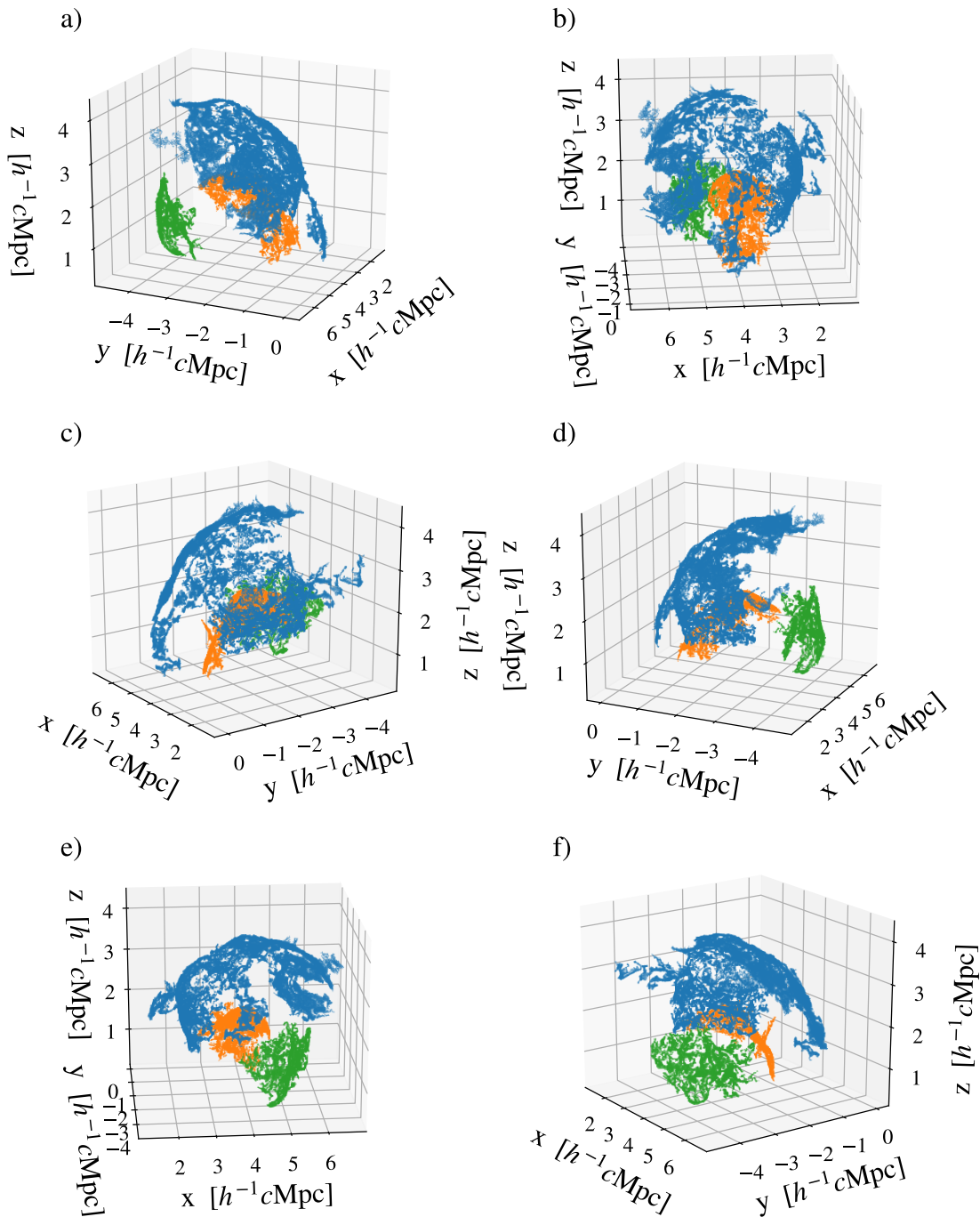


Figure A.28: FoF on raw data set *a) - f)*) Full rotation in 60° steps.

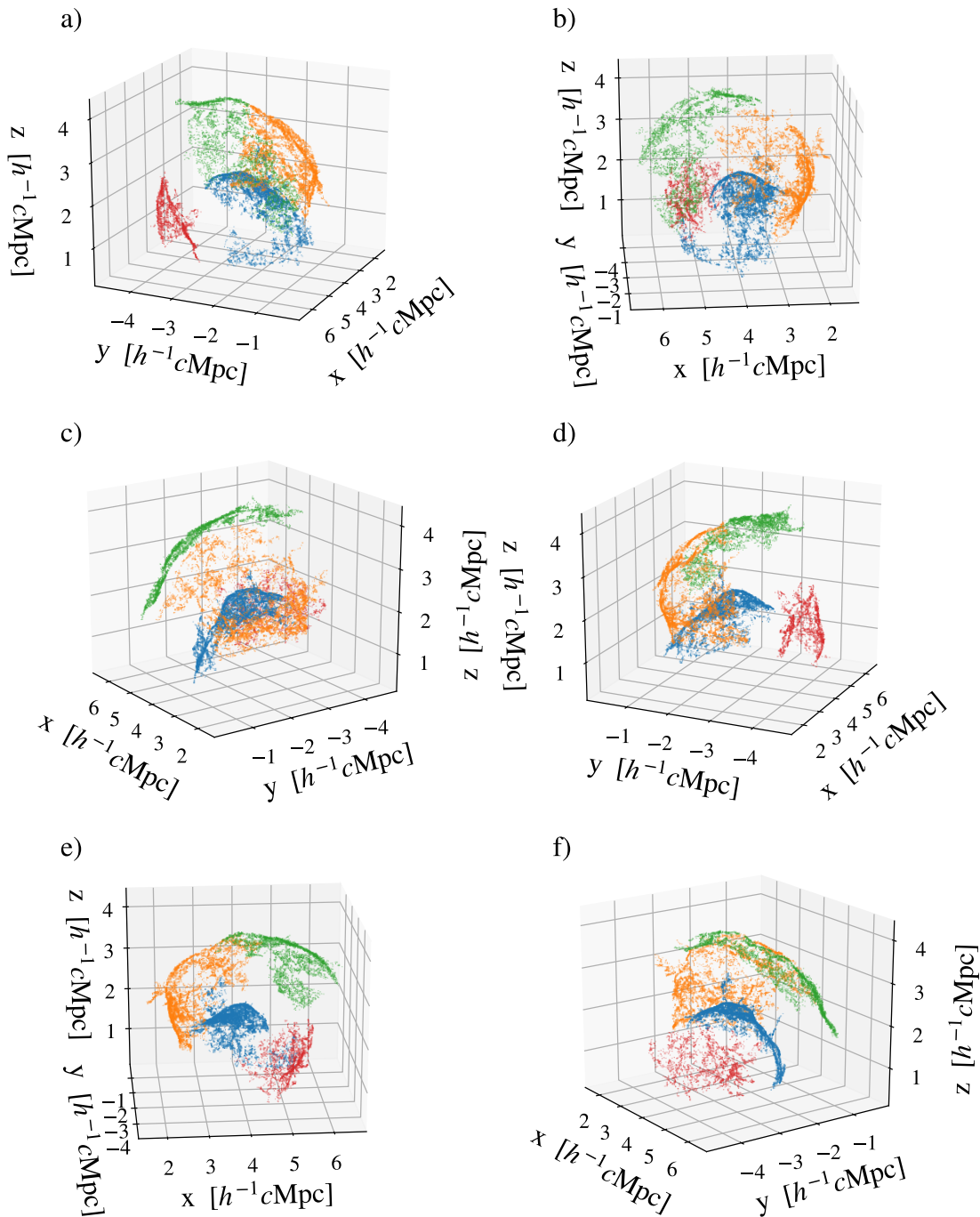


Figure A.29: FoF on denoised data set *a) - f)* Full rotation in 60° steps.

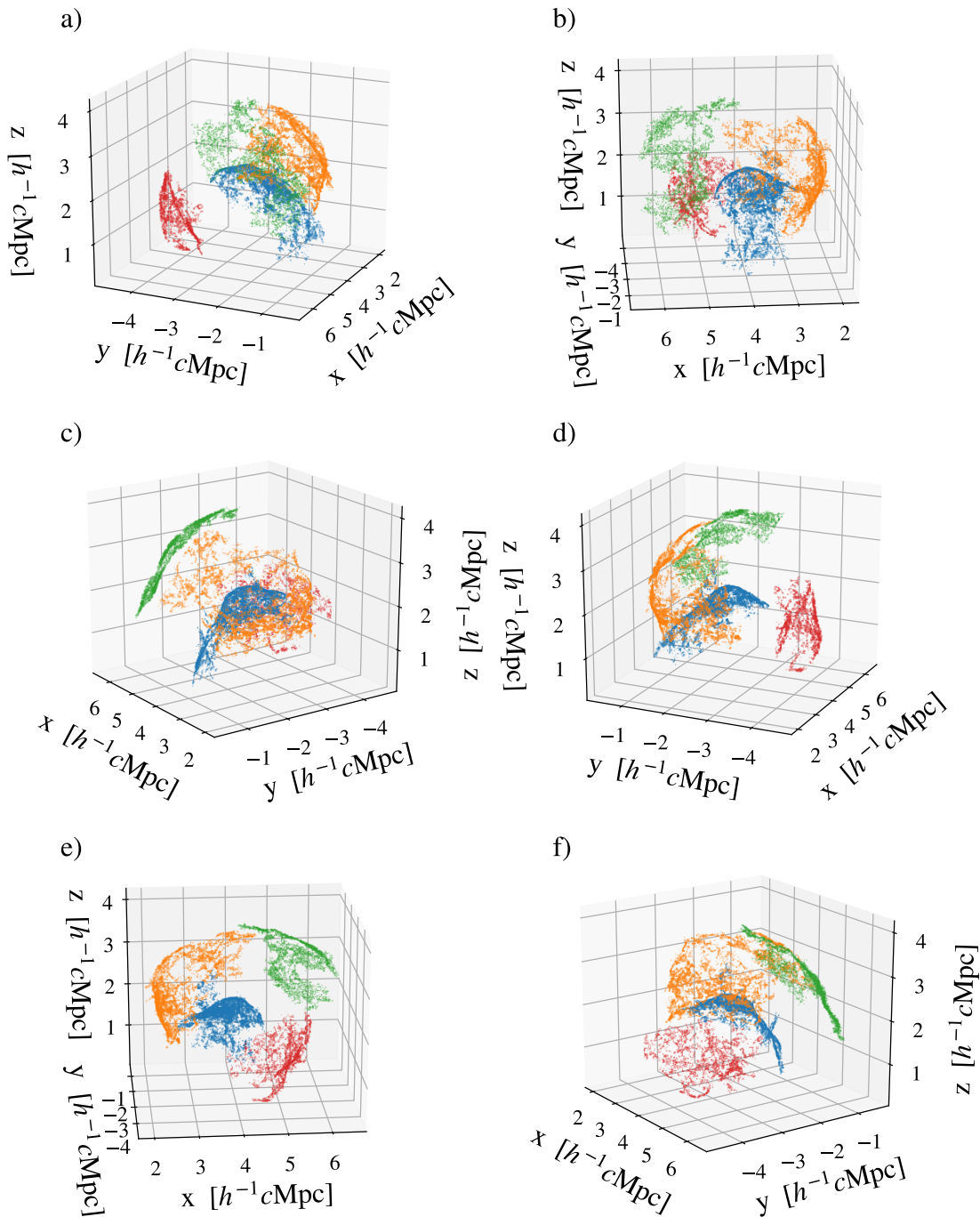


Figure A.30: DBSCAN in space a) - f) Full rotation in 60° steps.

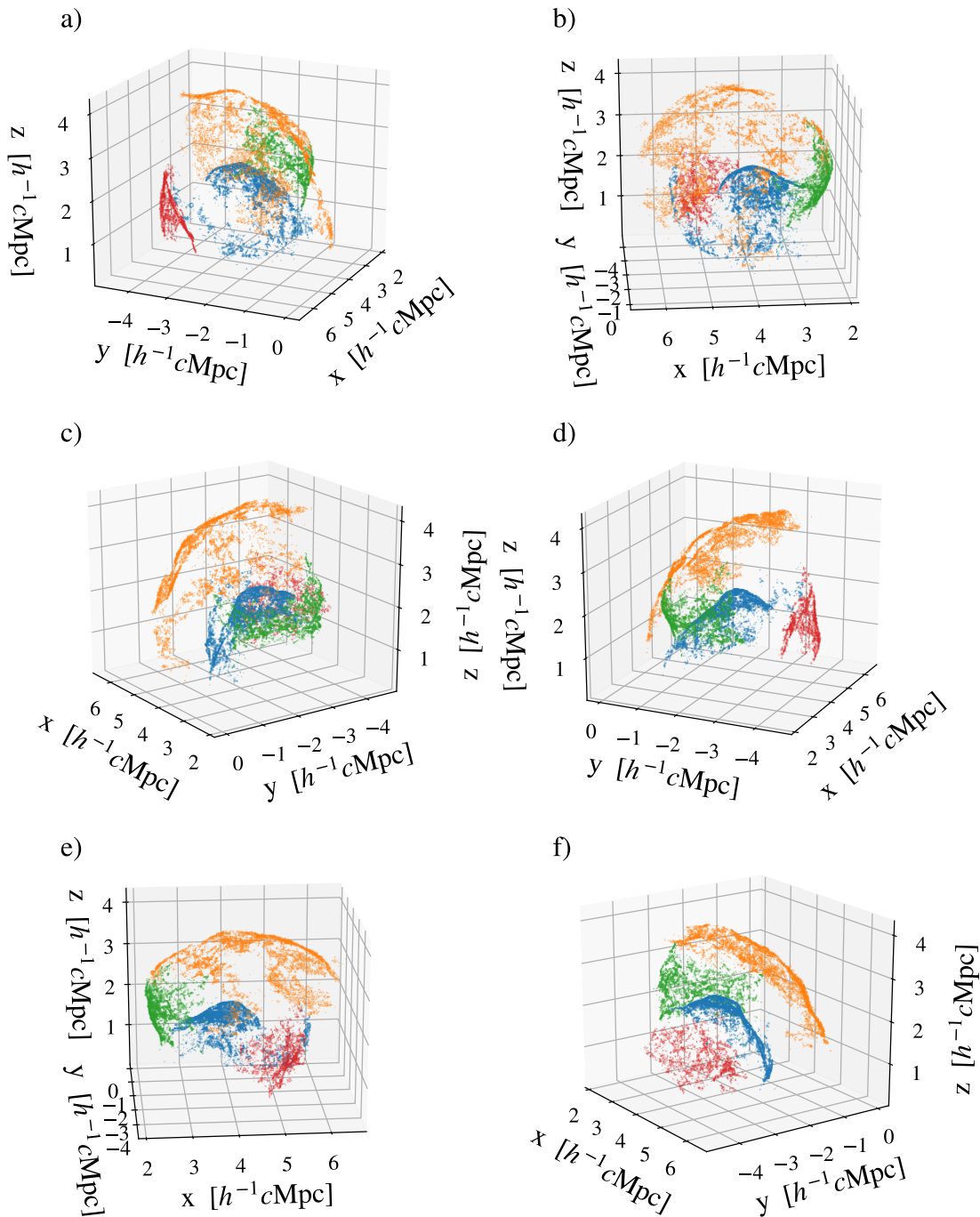


Figure A.31: DBSCAN in space and norm a) - f) Full rotation in 60° steps.

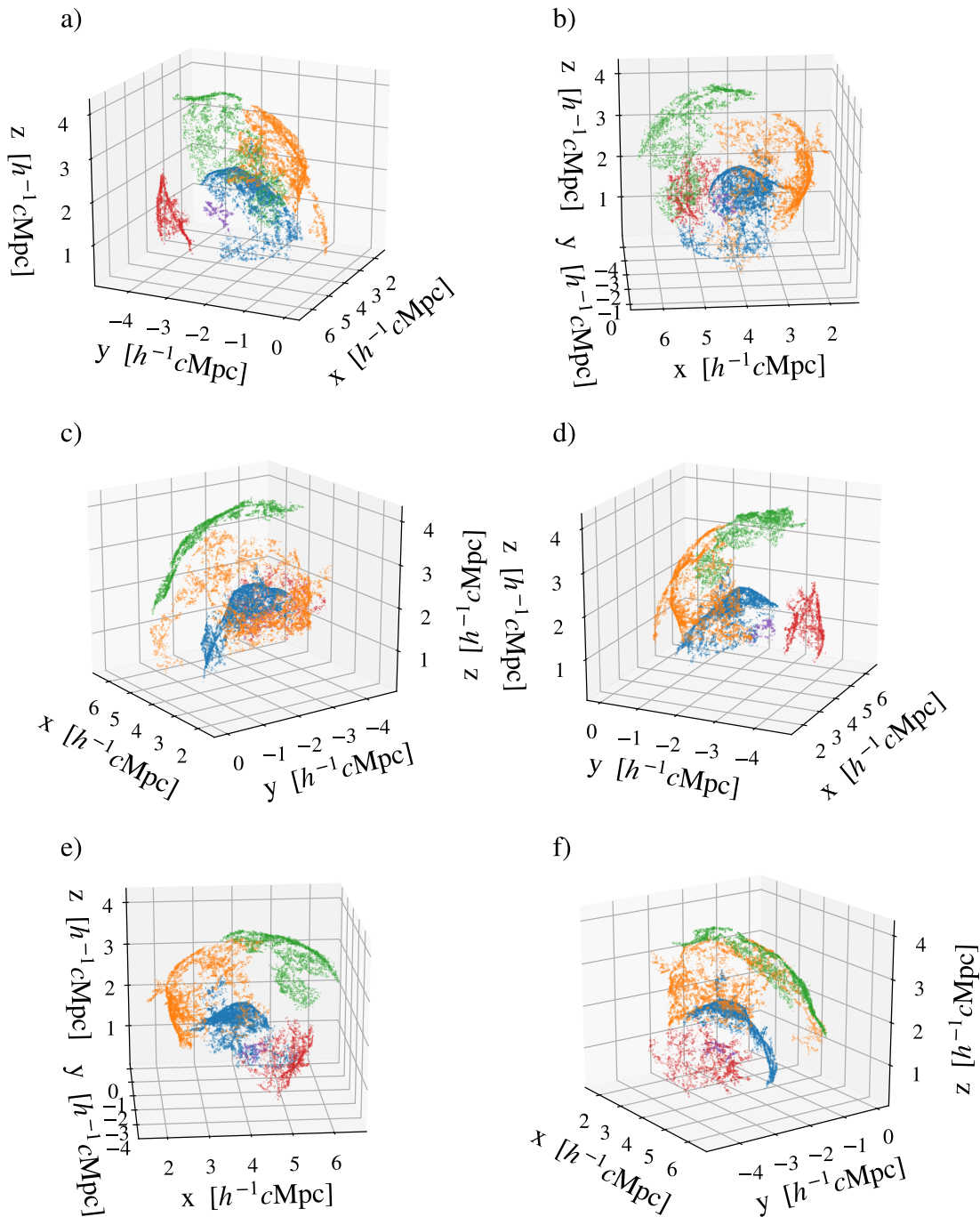


Figure A.32: DBSCAN in space after denoising a) - f) Full rotation in 60° steps.